Sanjiv Kumar and Candida F. Dewes contributed equally to the work.

Key Points:

- Effects of global warming on soil moisture variability are relatively small or even decrease despite increasing precipitation variability
- Reduction in soil moisture memory counteracts the effect of increasing El Niño-Southern Oscillation and teleconnected precipitation variability
- Regional mean state soil moisture changes drive future drought and pluvial risks

Supporting Information:

Supporting Information may be found in the online version of this article.

Correspondence to:

S. Kumar,
szk0139@auburn.edu

Robust Changes in North America's Hydroclimate Variability and Predictability

Sanjiv Kumar[1] , **Candida F. Dewes[2,3]** , **Matthew Newman[4]** , **and Yanan Duan[1]**

[1]Geospatial and Environmental Informatics, College of Forestry, Wildlife and Environment, Auburn University, Auburn, AL, USA, [2]Cooperative Institute for Research in Environmental Sciences, University of Colorado, Boulder, CO, USA, [3]National Snow and Ice Data Center, University of Colorado, Boulder, CO, USA, [4]NOAA Physical Science Laboratory, Boulder, CO, USA

Abstract Climate change adaptation planning requires a robust understanding of the projected change in hydroclimate variability and predictability. We use two large ensemble data sets to quantify the projected change in land hydroclimate variability and its potential predictability. Additionally, we use a "reddened El Niño-Southern Oscillation (ENSO)" framework that partitions annually averaged root-zone soil moisture variability into ENSO, land surface memory, and internal variability to understand drivers of the changes in hydroclimate variability and predictability. Even when global warming is projected to increase ENSO and its teleconnected precipitation variability over North America, we find that the corresponding change in soil moisture variability is relatively small and even decreases. This counter-intuitive result occurs since there is also a concurrent projected reduction in land surface memory due to global warming, which leads to reduced year-to-year persistence of soil moisture variability. Further, we find that regional mean state land surface (soil moisture) changes primarily drive future drought and pluvial risks, suggesting that infrastructure planning can incorporate robust mean state changes despite uncertainty in the variability projections. For the regions and in the models where the ENSO signal increases, we also find a concomitant shift in the frequency of drought and pluvial events, with higher power on inter-annual time scales but less power on decadal time scales, enhancing inter-annual hydroclimate predictability.

Plain Language Summary A 22-year-long drought (megadrought) has lowered Lake Mead's water level to its lowest level, threatening the water supply to the millions of people in the US Southwest. Land surface integrates year-to-year precipitation variability with storage in soil and vegetation-atmosphere interaction processes, giving rise to long-term regional hydroclimate variability as seen in Lake Mead's water-level record. However, projections of regional hydroclimate variability are highly uncertain due to the model's biases, internal variability, and structural uncertainty among climate models. Therefore, we use a very large number of simulations and synthetic data from two different climate models to assess the hydroclimate variability robustly. We find that year-to-year variation in precipitation increases with global warming. However, the corresponding soil moisture variability changes are small or even decreased. This occurs because of a decreased year-to-year persistence in land surface conditions (memory) due to global warming. An important implication is that the regional mean state (soil moisture) changes are the primary drivers of future drought and pluvial risks. Therefore, the water resources planning may include mean-state-driven hydroclimatic changes despite uncertainty in the variability projections.

1. Introduction

The land hydroclimate integrates precipitation and temperature inputs with soil and land use/land cover (vegetation) processes, providing a societally relevant quantity, for example, drought and pluvial risks. Understanding how decadal climate variations impact land hydroclimate extremes remains challenging, with numerous uncertainties in the climate system still to be adequately assessed (Bellucci et al., 2015; Meehl et al., 2014; Merryfield et al., 2020; Stouffer et al., 2017), including the relative importance of oceanic variability, internal atmospheric dynamics, and land-atmosphere interaction processes (Kumar et al., 2020; Schubert et al., 2016). In North America, El Niño-Southern Oscillation (ENSO) strongly affects land hydroclimate variability and predictability (DelSole et al., 2014; Fasullo et al., 2018; Newman et al., 2016) through its atmospheric teleconnections (Ault et al., 2018; Newman et al., 2016), including modulating long-term drought risks in the Southwest United States (Stevenson et al., 2018). In California, for example, positive ENSO phases increase wintertime pluvial risk, while

drought risk increases with ENSO's negative phases (Kam & Sheffield, 2016). Inter-annual memory in the deep soil layer and groundwater could also enhance long-term drought and pluvial events and predictability (Kumar et al., 2019; Schubert et al., 2008; Sutton et al., 2021). A recent study suggested that internal climate variability alone could cause persistent drought lasting up to several decades, also known as megadrought (Ault et al., 2018).

Anthropogenic climate change can increase the risk of drought and pluvial extremes. For example, in California, where the global warming effect could be compounded by below-normal precipitation, megadrought risk has been projected to increase (Diffenbaugh et al., 2015). In addition, ENSO and its teleconnected precipitation anomalies may strengthen in future warming scenarios (Yun et al., 2021), further impacting land hydroclimate variability (Fasullo et al., 2018). However, the effects of climate change on ENSO variability are model-dependent (Stevenson et al., 2021), and signals are often small enough that large-ensemble climate simulations are required to assess ENSO changes robustly (Maher et al., 2018; J. Singh et al., 2022). Therefore, we employ two large ensemble climate data sets (CESM-LE and GFDL-CM3-LE) to bring out the robust features of the projected change and develop a conceptual framework (next paragraph) to understand its drivers and associated risks. Additionally, we evaluate the extent to which changes in drought and pluvial risks in the future climate depend upon changes in the mean state or the variability.

Some critical aspects of climate variability can be represented by a slow dynamical system (e.g., an ocean or land surface layer) forced by relatively fast weather noise, yielding a low-frequency or "reddened" climate signal (Frankignoul & Hasselmann, 1977). This view has been expanded to include more coherent forcing sources, for example, ENSO. For example, a comparison to a "Reddened ENSO" null hypothesis is useful for decadal variability of North Pacific sea surface temperature (SST; Newman et al., 2016) and North American drought indices (Ault et al., 2018). Therefore, we employ a Reddened ENSO framework to evaluate how projected changes in both ENSO and land surface memory can impact hydroclimate variability and predictability in North America.

We represent land hydroclimate using the root zone (surface to 1 m deep) soil moisture anomalies, whose dynamics integrate the effects of land and climate processes (Cook et al., 2020; A. Singh et al., 2020). Other metrics, such as PDSI (Sheffield et al., 2012), are significantly correlated with soil moisture variability (Figure S1 in Supporting Information S1). Most plant roots, including 96% of crop roots, 94% of evergreen needle leaf trees' roots, and 93% of deciduous broadleaf trees' roots, are found in the top 1m soil layer (Amenu et al., 2005; Kumar et al., 2019; Zeng, 2001).

2. Data and Methods

We used two large ensemble climate simulations to assess projected changes in North America's hydroclimate variability and predictability. Next, we developed the Reddened ENSO framework to diagnose the drivers of the projected change. We evaluate the Reddened ENSO framework using observations from ERA5-Land soil moisture (Muñoz-Sabater et al., 2021) and Berkeley Earth SST data (Rohde & Hausfather, 2020). Finally, we use the Reddened ENSO framework to generate a very large ensemble of synthetic soil moisture data and assess the robust changes in the hydroclimate extremes.

2.1. Large Ensemble Climate Data (CESM-LE and GFDL-CM3-LE)

We investigate how hydroclimate variability changes within two large ensemble experiments: the 40-member Community Earth System Model Large Ensemble (CESM-LE) (Kay et al., 2015) and a 20-member ensemble experiment with the Geophysical Fluid Dynamics Laboratory's Coupled Model version 3, generated at the NOAA Physical Science Laboratory (GFDL-CM3-LE) (Milly et al., 2014; Sun et al., 2018). Both large ensemble experiments covered the years 1920–2100, where each ensemble member was subjected to the same radiative forcing scenario (historical up to 2005 and Representative Concentration Pathway 8.5 thereafter) but began from slightly different initial atmospheric states. The analyses were carried out on five consecutive, non-overlapping 30-year periods, from 1940 to 1969, 1970–1999, 2000–2029, 2030–2059, and 2060–2089, with 1970–1999 as the reference climate period. For brevity's sake, we show the spatial pattern for the reference climate period and the changes in projection periods: 2030–2059 and 2060–2089 periods (e.g., Figure 1). Scatter plots show changes in all five climate periods and ensemble members (e.g., Figure 2).

We focus mainly on two variables, monthly tropical SST (between 30°S and 30°N) and monthly top 1-m soil moisture across North America, but we also use precipitation to bring out novel aspects of our results. We first
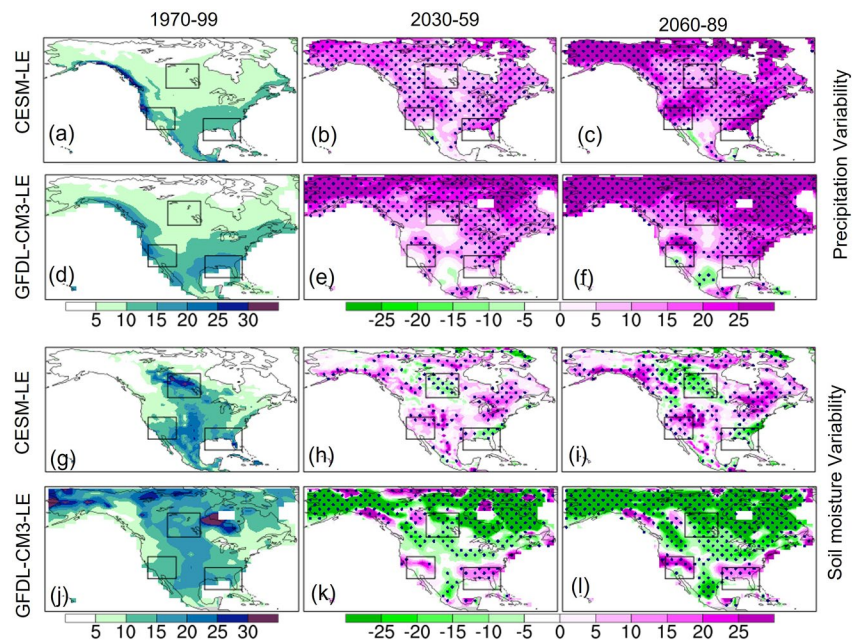
Figure 1. Hydroclimate variability projections in two large ensemble data sets. The figure compares precipitation variability changes with the corresponding change in soil moisture variability. Notice a smaller increase or decrease in soil moisture variability compared to corresponding precipitation changes. The left column shows inter-annual variability in the historical climate and the respective climate model, and the middle and right columns show the projected change in % unit. For the left column, the precipitation unit is mm/month, and the soil moisture unit is mm of water per 1 m soil depth. Ensemble mean values shown are from 40 ensemble members in CESM-LE and 20 in GFDL-CM3-LE projections. Stippling denotes statistically significant differences at a 95% confidence level using the *F*-test.

applied a 12-month running mean filter to the monthly time series for each variable so that our analysis focuses on annual and longer time scales. Next, we computed the ensemble mean by averaging the time series across ensemble members and applying a 21-year filter separately across all January, February, and so on, thus preserving both
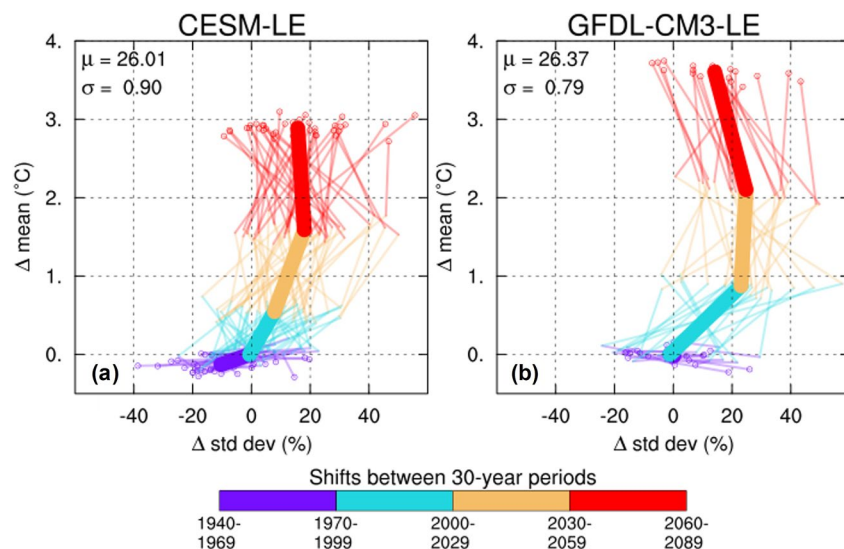

Figure 2. Changes in mean and variance of Niño 3.4 sea surface temperature (SST). Scatterplots show 30-year shifts in mean and standard deviation Niño 3.4 SST relative to the 1970–1999 period. Thin-colored lines denote the shift of individual ensemble members between two 30-year periods, while the thick-colored line represents the ensemble mean. Values for μ and σ (at the top right corner of each scatterplot) denote the ensemble mean's 1970–1999 mean and standard deviation, respectively. Notice the projected increase in El Niño-Southern Oscillation variability in both climate models.

the annual cycle and the 180-year modeled trend within the ensemble mean. Then we computed anomalies by subtracting this ensemble mean from the monthly values. Finally, we independently computed the empirical orthogonal functions (EOFs) of monthly tropical SSTs for every 30 years and used the principal component of the leading mode (i.e., ENSO) as the ENSO index in our analysis.

2.2. Reddened-ENSO Framework

To investigate the effects of climate change on hydroclimate variability and predictability within the two large ensembles, we developed a simple multivariate regression model of the yearly (12-month mean) soil moisture anomalies $S_{(t)}$ using two predictors—concurrent ENSO $[E_{(t)}]$, and previous year's soil moisture anomalies $[S_{(t-12)}]$, referred to as the "Memory" as follows:

$$S_{(t)} = \alpha \, S_{(t-12)} + \beta \, E_{(t)} + \varepsilon \tag{1}$$

Here, α and β are regression coefficients representing the Memory and ENSO effects, ε is the noise term determined as a residual using respective climate model data (discussed later). $S_{(t-12)}$ represents the previous year's soil moisture anomalies. We refer to Equation 1 as the "Reddened ENSO framework." Newman et al. (2003) introduced this framework to diagnose how ENSO drives year-to-year variability in the North Pacific, where the memory term, in that case, represented oceanic mixed layer processes.

Time averaging (coarse-graining) can allow more complex climate dynamical systems to be represented by simple noise-forced linear systems (Equation 1), as demonstrated in many previous studies starting with Hasselmann (1976) (Ault et al., 2018; Hasselmann, 1976; Newman et al., 2003; Penland & Sardeshmukh, 1995). In Equation 1, the evolution of the current year's soil moisture variability $S_{(t)}$ depends on the previous year soil moisture anomalies $S_{(t-12)}$; that is, without ENSO forcing it is represented by a first-order Markov process (Amenu et al., 2005; Chikamoto et al., 2015; Delworth & Manabe, 1988; Schlosser & Milly, 2002). We also assume that ENSO can be "perfectly" known for the given year, which is not entirely accurate for real-world ENSO predictions (Ding et al., 2018; Ham et al., 2019). Additionally, for this simple model, we assume that: (a) the interactions between $S_{(t-12)}$ and $E_{(t)}$ are negligible (Figure S2 in Supporting Information S1); and (b) the errors are normally distributed and not serially correlated (Figures S3 and S4 in Supporting Information S1).

We test the ability of the Reddened ENSO framework (Equation 1) to capture soil moisture variability and predictability in each of the large ensembles. To derive the error and the coefficients α, and β, we first standardized the soil moisture and ENSO variables by their respective standard deviations, computed across all ensemble members and all five 30-year periods. Next, we computed separate regression models for each period. Finally, we employed a cross-validation technique that takes advantage of the multiple ensemble members to produce more robust regression coefficient estimates and more realistic errors. We computed the regressions (Equation 1) 40 times for CESM-LE (20 times for GFDL-CM3-LE), each iteration using 39 (19) ensemble members to compute the coefficients and the remaining member to predict the soil moisture anomaly, as well as the error and goodness-of-fit metrics.

2.3. Potential Predictability Metric

The signal-to-total noise ratio (S/T) is computed as follows. From Equation 1, the predicted soil moisture signal $\hat{S}_{(t)}$ and the noise term ε are as below:

$$\widehat{S_{(t)}} = \alpha \, S_{(t-12)} + \beta \, E_{(t)} \tag{2}$$

$$\varepsilon = S_{(t)} - \widehat{S_{(t)}} \tag{3}$$

where $S_{(t)}$ is the soil moisture anomaly in the climate model (*observed*), $E_{(t)}$ is the ENSO amplitude in the climate model, and α and β are the regression coefficients computed using the cross-validation technique described previously. Hence, the S/T is given by:

$$S/T = \left(\frac{variance\left(\widehat{S_{(t)}}\right)}{variance(\varepsilon) + variance\left(\widehat{S_{(t)}}\right)} \right)^{0.5} \tag{4}$$

We determined the statistical significance of the signal variance by comparing it with the noise variance using the F-test described by Guo et al. (2011). The actual skill is the anomaly correlation between $\widehat{S_{(t)}}$ and $S_{(t)}$. The actual skill and the potential predictability are very similar in this study (Figure S5 in Supporting Information S1) because of the perfect model design, that is, α and β are computed from the large ensemble climate data and validated using the withheld ensemble.

2.4. Soil Moisture Memory and Effects of Global Warming

We computed soil moisture memory as its e-folding decay time scale (τ, Equation 5), representing the land surface reddening effect of the white noise precipitation forcing. The soil moisture memory drives a red spectrum in soil moisture variability (Chikamoto et al., 2015; Kumar et al., 2019).

$$\frac{ds}{dt} = -(^1/_\tau)s + \varepsilon \tag{5}$$

Equation 5 is the first-order Markov process model for the root zone soil moisture (s) variability; τ is the soil moisture memory time scale computed using the best-fit exponential decay function from 1 to 24 months lead time as described in Kumar et al. (2019), and ε is the white noise.

To understand how global warming affects τ, Equation 5 can be compared with the classic water balance equation [$\Delta S = -ET + (P - R)$] where ET is evapotranspiration, P is precipitation, and R is runoff. Additionally, ET can be written as a function of soil moisture, and potential evapotranspiration (PET) [ET = f(s)*PET] and $(P - R)$ can be treated as white noise (ε). After doing some algebra, it can be shown that $\tau \propto \frac{1}{PET}$, that is, soil moisture memory is inversely related to PET, for example, midlatitude regions have higher memory than tropical regions (Delworth & Manabe, 1988). As global warming increases PET (Dewes et al., 2017; Kumar et al., 2016), soil moisture memory can decrease.

3. Results

We analyzed the impacts of global warming on projections of soil moisture variability and compared them with the projected changes in precipitation and ENSO variability (Section 3.1). Next, we developed and validated the Reddened ENSO framework using long-term historical observations (Section 3.2). We employed the Reddened ENSO framework to understand changing hydroclimate variability and predictability and their drivers (Section 3.3). Finally, we assess the implications of the changing hydroclimate variability on long-term drought and pluvial risks and hydrologic design (Section 3.4).

3.1. A Smaller Projected Change in Soil Moisture Variability Relative to the Increased Precipitation and ENSO Variability

Projected change in soil moisture variability is relatively small, or even decreases, despite a significant increase in the precipitation variability (Figure 1). Both climate models, CESM-LE and GFDL-CM3-LE, show a robust increase in precipitation variability, which strengthens with the global warming signal, that is, precipitation variability is stronger in the 2060–2089 period compared to the 2030–2059 period. During the 2060–2089 period, North America's precipitation variability increased by $16.5 \pm 6.5\%$ and $18.5 \pm 8.5\%$ in CESM-LE and GFDL-CM3-LE, respectively. The corresponding changes in soil moisture variability are $3.7 \pm 6.4\%$ and $-12.7 \pm 8.1\%$, respectively. These estimates are for the 2060 to 2089 period relative to the 1970–1990 period; $X \pm Y$ shows ensemble mean (X) and inter-ensemble spread represented by two times standard error estimates calculated from 40 (20) ensemble members of the CESM-LE (GFDL-CM3-LE). GFDL-CM3-LE projects a robust decrease in soil moisture variability for most high-latitude regions and parts of the central United States. CESM-LE also shows a decrease in soil moisture variability in the Canadian Plains and parts of the Southeast United States. In the Southwest United States, and during the 2060–2089 period, the CESM-LE showed a 50% smaller increase in soil moisture variability ($8.9 \pm 6.5\%$) than precipitation variability increase ($17.6 \pm 7.7\%$).

Increased precipitation variability is consistent with an increase in ENSO variability in CESM-LE and GFDL-CM3-LE, although note that in GFDL-CM3-LE, ENSO amplitude declined in the latter half of the 21st century. Figure 2 shows the projected change in Niño 3.4 SST mean and its variability using the line scatter

plot with changes from one period to the next indicated by line segments ranging from blue (early) to red (late). We constructed the Niño 3.4 index for individual ensemble members and the ensemble mean every 30 years by averaging the SST anomalies in the Niño 3.4 region. The maximum increase in the ensemble mean ENSO index variability is found during the 2030–2069 period, and they are 17.9 ± 4.5% for CESM-LE and 24.7 ± 6.1% for GFDL-CM3-LE. Then, it slightly decreases to 15.8 ± 4.7% in CESM-LE and considerably decreases to 14.1 ± 6.1% in GFDL-CM3-LE during the 2060–2089 period.

Internal climate variability can cause considerable changes in ENSO variability, that is, individual ensemble member responses can be higher (or lower) than the ensemble mean responses discussed in the last paragraph. For example, individual ensemble members show ENSO variability increases up to 55.6% in CESM-LE and 57.5% in GFDL-CM3-LE (see maximum scatter spread in Figure 2), 2–3 times larger than the corresponding ensemble-mean responses. Hence, the large ensemble mean allows us to assess mechanisms that might lead to robust hydroclimate variability changes due to global warming.

The large ensemble data sets of the CMIP6 (Coupled Model Intercomparison Project Phase 6) climate models also show increased ENSO variability under a global warming scenario (Maher et al., 2018; Rodgers et al., 2021). In addition, an increased ENSO-precipitation variability response is often present in climate models with an "El Niño-like" SST change in the tropical mean SST due to the nonlinear mean SST-rainfall relationship (Yun et al., 2021). However, there is some question as to whether climate models have correctly captured past trends in tropical mean SSTs (Power et al., 2021).

Precipitation variability can also change due to thermodynamics, that is, the Clausius Clapeyron relationship and circulation changes (Allan et al., 2020; Seager et al., 2010). However, this study aims to develop a predictive understanding of the changing hydroclimate. Hence, we investigate changes in ENSO and related hydroclimatic variability because ENSO has a long-lead predictability timescale (Gonzalez & Goddard, 2016).

3.1.1. Regional Changes in Soil Moisture Variability

Impacts of climate change on the soil moisture mean, and variance is geographically dependent. To explore this point, we constructed soil moisture indices for three regions: Southwest United States, Southeast United States, and Canadian Plains (see boxes in the maps of Figure 1). These regions represent diversity in the North American hydroclimate, for example, the humid subtropical climate in the Southeast versus dry climate in the Southwest and high-latitude climate in the Canadian Plains. The evolution of soil moisture means and variance for each region (relative to the "historical" 1970–1999 period) is shown using line scatter plots analogous to Figure 2 but for soil moisture indices (Figure 3).

For the Southwest United States, CESM-LE and GFDL-CM3-LE show qualitatively similar soil moisture drying trends (Figures 3a and 3b). However, the soil moisture drying is more substantial in GFDL-CM3-LE (−15.1 ± 0.9 mm) than in CESM-LE (−6.0 ± 1.0 mm) because of their diverging mean precipitation responses, where CESM-LE shows an increasing precipitation trend, and the opposite is found in GFDL-CM3-LE projections for the Southwest United States (Figure S6 in Supporting Information S1). This result illustrates different plausible climate outcomes due to structural uncertainty among models compared with the use of only one large ensemble in many previous studies (Diffenbaugh et al., 2015; Swain et al., 2018). In addition, uncertainties in the Southwest precipitation projections can be related to large-scale circulation changes, such as for the Pacific jet stream (Neelin et al., 2013) and ENSO-precipitation teleconnection patterns (Allen & Luptowitz, 2017).

The two climate models differ in the Southeast United States (Figures 3c and 3d), where the CESM-LE shows a soil moisture wetting trend (11.4 ± 0.7 mm) while the GFDL-CM3-LE shows a small soil moisture drying trend (−4.0 ± 0.6 mm). However, the corresponding soil moisture variability changes are insignificant: −3.3 ± 4.1% in CESM-LE and 1.8 ± 4.5% in GFDL-CM3-LE.

Both climate models project a significant decrease in soil moisture variability in the Canadian Plains: −9.2 ± 4.3% in CESM-LE and −21.6 ± 4.6% in GFDL-CM3-LE. However, the corresponding soil moisture mean change is minimal (Figures 3e and 3f), despite the projected increase in precipitation in the high-latitude regions (Figure S6 in Supporting Information S1). This result highlights the effect of global warming on soil moisture dynamics. Overall, the projected change in soil moisture variability is considerably smaller or even the opposite sign compared to changes in precipitation variability (also see Cook et al., 2020; Ukkola et al., 2020), warranting further investigation into its drivers and potential implication on drought and pluvial risks.
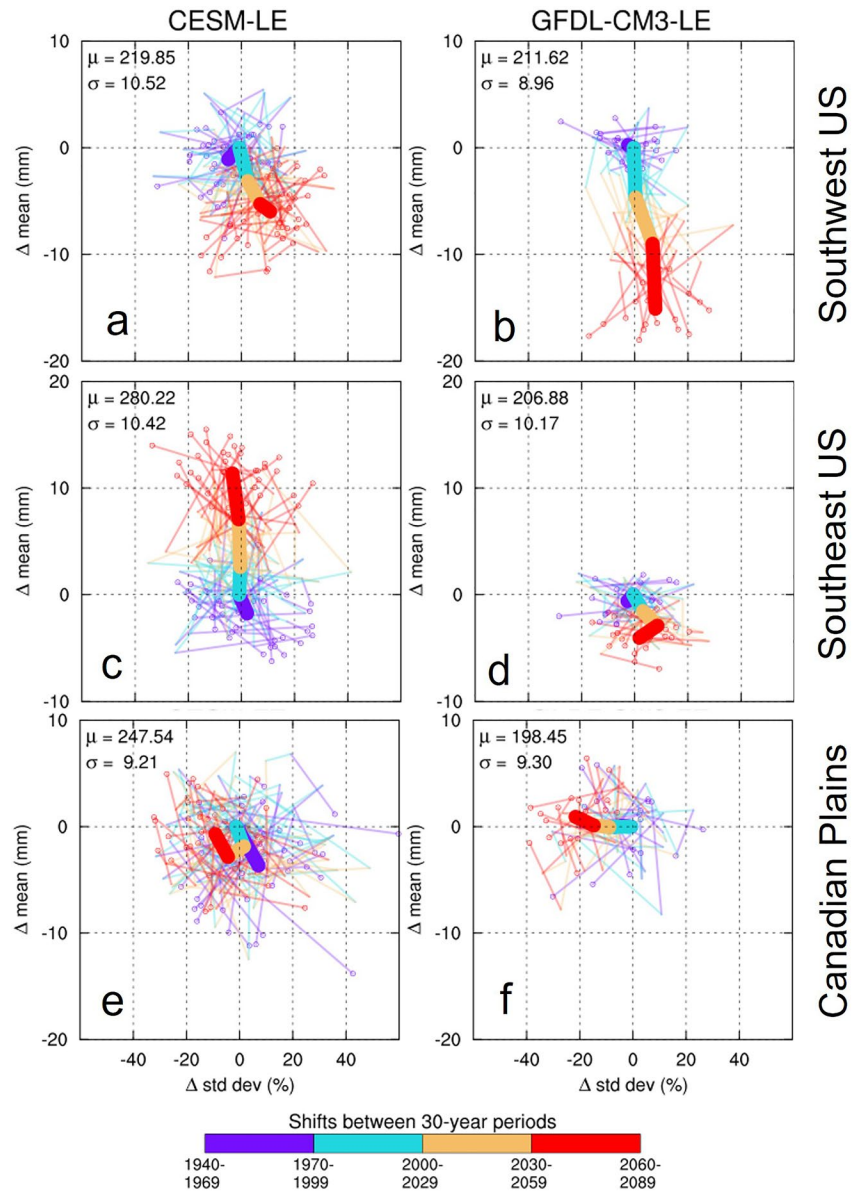
Figure 3. Regional changes in soil moisture mean and variability. Same as Figure 2 for soil moisture in Southwest United States, Southeast United States, and Canadian Plains shown by boxes in Figure 1.

3.2. Development and Validation of the Reddened ENSO Framework

3.2.1. Observed Hydroclimate Variability in North America

The coarse-graining of the time series (12-month running mean) captures some key observed hydroclimate variability features at inter-annual and longer time scales. For example, the observed time series of ENSO and soil moisture variations both capture two major transitions: the 1976/1977 transition that led to a multidecadal wet period during the 1980s and 1990s, and the 1998/1999 transition leading to a dry period during the 2000s to present (Figures 4b and 4c). These transitions have been identified in the literature (Dai et al., 2015; Meehl et al., 2016). For example, the first principal component of the SST variability in the Indian and tropical Pacific oceans (Figure 4a), referred to as ENSO, shows a transition from a negative phase to a positive phase during 1976/1977 and then again to a negative phase during 1998/1999. In addition, the tropical SST variability correlates very well with the National Oceanic and Atmospheric Administration's Niño 3.4 index with a correlation coefficient of 0.96. Correspondingly, ERA5-Land soil moisture variability shows multidecadal wet and dry
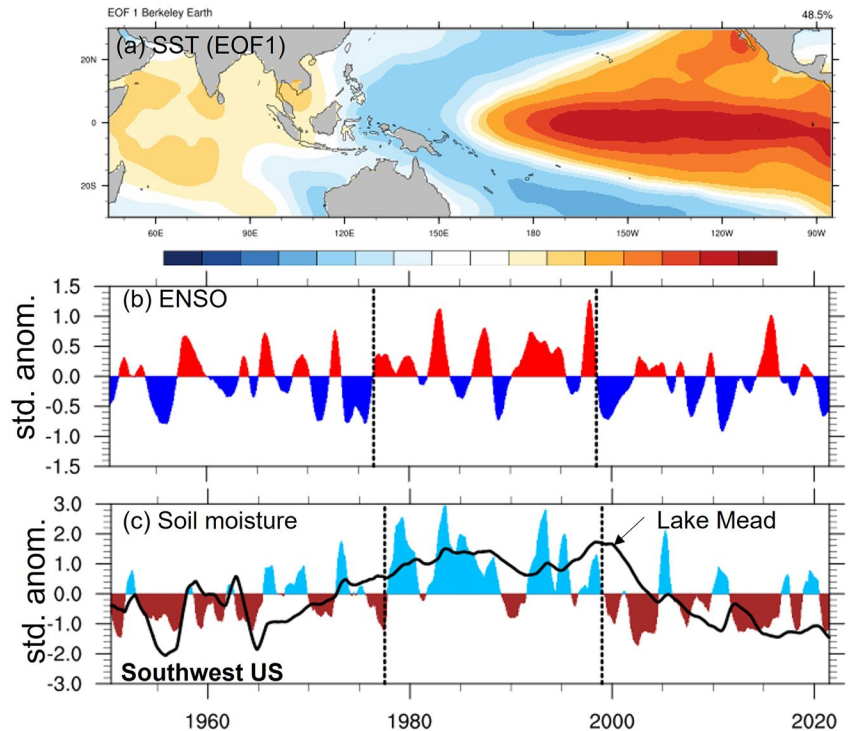
Figure 4. Observed hydroclimate variability in North America from 1950 to 2021. (a) First empirical orthogonal function (EOF1) of sea surface temperature (SST) variability in the Indo-Pacific domain calculated from the Berkeley Earth surface temperature data. EOF1 explains 48.5% variance in the detrended SST data (b) Principal component 1 (PC1) time series, representing an El Niño-Southern Oscillation (ENSO) index. The vertical dashed lines show two major Pacific Basin regime shifts: 1976/1977 and 1998/1999. (c) Standardized soil moisture anomalies in the Southwest United States calculated from the ERA5-Land reanalysis data. Lake Mead water level data is shown using the overlain black line. Notice the recent megadrought that started in the early 2000s and continues. Vertical line in panel (c) is lagged by 1 year from the corresponding vertical line in panel (b) to reflect soil moisture memory effects.

periods in the Southwest United States (Figure 4c). The soil moisture time series is obtained by averaging it over the Southwest box, same as in Figure 1.

3.2.2. Hydroclimate Modeling

Hydroclimate modeling requires incorporating the memory component (Barnett & Pierce, 2008; Hurst, 1951). For example, consider the historical Lake Mead water level variability shown using the black curve in Figure 4c. Located in the center of the Southwest United States, Lake Mead's water level shows a much higher persistence than the observed ENSO and soil moisture variability in the Southwest United States. One-year lag autocorrelations are 0.17, 0.41, and 0.91 for the observed ENSO, soil moisture, and Lake Mead water level records. In comparison, a correlation value of 0.20 or more is statistically significant at the 95% level using a one-sided t test and a 72-year-long data record (1950–2021) if each year is independent. Effects of the two major transitions and the recent megadrought are also evident in the Lake Mead water level data, which is significantly correlated with Southwest United States soil moisture variability (correlation coefficient: 0.47).

3.2.3. Long-Term Hydroclimate Prediction

A long-term hydroclimate prediction (1 year or longer) is rather challenging because much of the forecast skill drops beyond the seasonal time scale (Meehl et al., 2021). For example, Figure 5a shows year-1 soil moisture forecast skill in state-of-art Seasonal to Multi-Year Large Ensemble (SMYLE) forecast (Yeager et al., 2022). We compare the drift-corrected SMYLE forecast anomalies (Kumar et al., 2014) with that in the ERA5-Land soil moisture data from 1970 to 2021. The SMYLE forecasts generally show statistically significant skill in the Western and Central United States. For the Southwest United States, one of the more predictable regions, the area
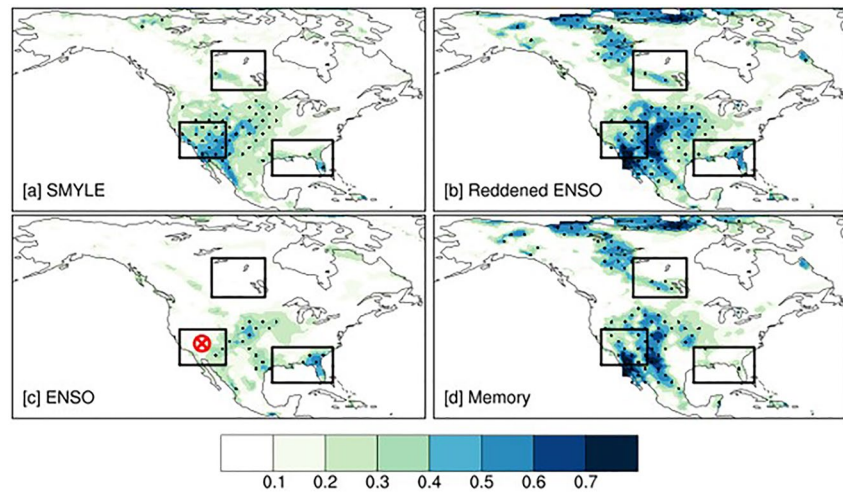
Figure 5. Evaluation of the Reddened El Niño-Southern Oscillation (ENSO) framework using observations and its comparison with the dynamical prediction system (SMYLE). (a) Year 1 (lead 1-to-12-month average) soil moisture forecast skill (anomaly correlation) in the dynamical prediction system. (b) Anomaly correlation between predicted soil moisture anomalies using Reddened ENSO model (Equation 1), and ERA5 soil moisture observations from 1950 to 2021, the same for (c) ENSO-only model, and (d) Memory only model. Stipplings denote a statistically significant correlation at a 95% confidence level. In panel (c), the red circle represents Lake Mead's location. Note: SMYLE data are available for 10-cm soil moisture, and from 1970 to 2019. We used 1 May and 1 November initialization date in SMYLE runs.

average anomaly correlation skill in the SMYLE forecast is 0.41, which is less than the common threshold for "useful" skill, that is, 0.50 (Pegion et al., 2019).

Interestingly, the Reddened ENSO framework reproduces much of the dynamical prediction skill, or even better (compare Figures 5a and 5b). We performed 12-fold cross-validation, where for each fold, we developed the model coefficients (Equation 1) using 92% of the data, validated it by making 1-year "forecasts" upon the with-held 8% data, and repeated the process 12 times to sample all the data. Since ERA5-Land soil moisture data are available for 72 years (1950–2021), we selected 6 years as the withheld data period for each iteration, giving 12 interactions. The methodology maximizes the sample size for estimating α and β coefficients (Equation 1) using observations with only one ensemble, unlike the large ensemble climate model data. For the Southwest United States, the area-averaged anomaly correlations between predicted and observed soil moisture anomalies are 0.45 in the Reddened ENSO model, comparable to or even better than the dynamical prediction skill. The lower skill in the SMYLE forecast might be due to a shallower soil layer (10 cm only available) and/or model biases and feedback (Esit et al., 2021). Overall, the Reddened ENSO framework provides a skillful soil moisture prediction in most of the conterminous United States except for the Northeast and the high-latitude regions consistent with the dynamical prediction system, that is, SMYLE.

Additionally, we can individually diagnose the ENSO and Memory components' contribution using the Reddened ENSO framework. We recalibrated the model (Equation 1) using Memory only ($S_{(t)} = a\,S_{(t-12)} + \varepsilon_a$), and ENSO-only ($S_{(t)} = b\,E_t + \varepsilon_b$) predictors, referred to as the components-only model, in further discussion. The ENSO and Memory-only component model's skills are shown in Figures 5c and 5d, respectively. Memory contributions are greater than the ENSO, emphasizing the memory's importance in North American hydroclimate modeling and prediction. Also, their contributions are spatially separated, generally. For example, Memory contributes most in the Southwest United States (anomaly correlation = 0.38), while ENSO contributes most in the Southeast United States (anomaly correlation = 0.30) (Figures 5c and 5d). This latter result is consistent with the ENSO-related precipitation signal during the cold season, which is the strongest in the Southeast United States and the central United States, extending from the Arizona-New Mexico border into Nebraska (Newman et al., 2016). Memory also contributes to the skill in the high-latitude regions, where ENSO's contribution is minimal. Overall, the Reddened ENSO framework is a valuable diagnostic tool for understanding long-term hydroclimate variability and predictability. Next, we use the Reddened ENSO framework to understand the drivers of changing hydroclimate variability and predictability.

3.3. Hydroclimate Variability and Predictability Under Global Warming

The Reddened ENSO framework shows strengthening and weakening of the hydroclimate predictability related to ENSO and memory components, respectively (Figures 6–8). As expected, the Reddened ENSO framework is more skillful in the perfect model setting (Figure 6) than in observations (Figure 5b). For example, the predictive skill in the 1970–1999 climate and CESM-LE data are 0.60, 0.45, and 0.39 for the Southwest United States, Southeast, and Canadian Plains.

The Reddened ENSO framework using GFDL-CM3-LE generally shows a higher skill in the high-latitude regions than the CESM-LE in the historical climate (Figures 6a and 6c). However, global warming causes a reduction in potential predictability in high latitudes, particularly in the GFDL-CM3-LE projections (compare Figure 6c with Figure 6d). For example, the potential skill in the Canadian plains and GFDL-CM3-LE model decreases from 0.40 in the 1970–1999 climate to 0.31 in the 2060–2089 climate. The corresponding potential skill in CESM-LE is 0.39 and 0.35, respectively.

Memory reduction primarily contributes to the reduction in potential skills. We find a widespread reduction in memory coefficient term (α) in the high-latitude regions, particularly in GFDL-CM3-LE projections (Figures 7e and 7f). The CESM-LE projections show a reduction in the memory coefficient term, too. For example, in the Canadian plains, α decreases from 0.40 to 0.31 in GFDL-CM3-LE projections and 0.38 to 0.32 in the CESM-LE projections.

The CESM-LE projections show a slight strengthening of the potential skill (1-year forecast skill) in the Southwest and Southeast United States under the global warming scenario (Figure 6). For example, the potential skill in the Southwest United States increases from 0.60 in the 1970–1999 climate to 0.66 in the 2060–2089 climate; and similarly for Southeast United States from 0.45 to 0.52 (Figures 6a and 6b). However, the potential skill remains similar or decreases slightly in the GFDL-CM3-LE projections (Figures 6c and 6d). For example, the GFDL-CM3-LE projections show a decrease in potential skill from 0.41 to 0.34 in the Southeast United States. The GFDL-CM3-LE shows a generally smaller potential skill than CESM-LE in the Southwest United States.

Impacts of ENSO (β coefficient in Equation 1) on hydroclimate predictability strengthen with global warming, particularly in the CESM-LE projections. For example, the β coefficient increases from 0.47 to 0.59 in the Southwest United States and 0.37 to 0.41 in the Southeast United States in the CESM-LE projections (Figures 7c and 7d). A slight increase from 0.30 to 0.33 is also found in the GFDL-CM3-LE projections for the Southwest United States (Figures 7g and 7h). However, GFDL-CM3-LE projections show the same β coefficient values (0.49) in the 1970–1999 and 2060–2089 climate in the Southeast United States. Both models show a minimal impact of ENSO on the Canadian Plains' soil moisture variability.
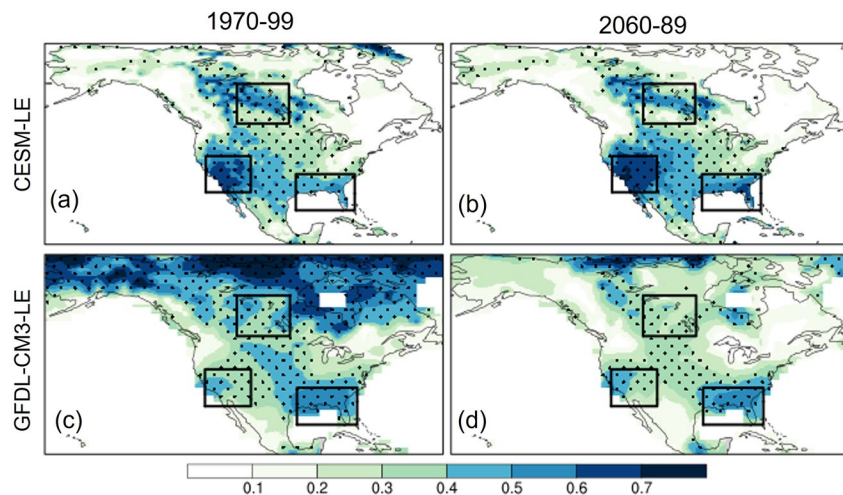

Figure 6. Effects of climate change on hydroclimate predictability using Reddened El Niño-Southern Oscillation framework. The figure compares the potential predictability of soil moisture between 1970–1999 and 2060–2089 climate and two large ensemble data. The signal to total variance metric represents the potential skill. Notice the strengthening of the predictability in the Southwest United States and CESM-LE projections and the weakening of predictability in the high latitude regions, particularly in GFDL-CM3-LE projections.
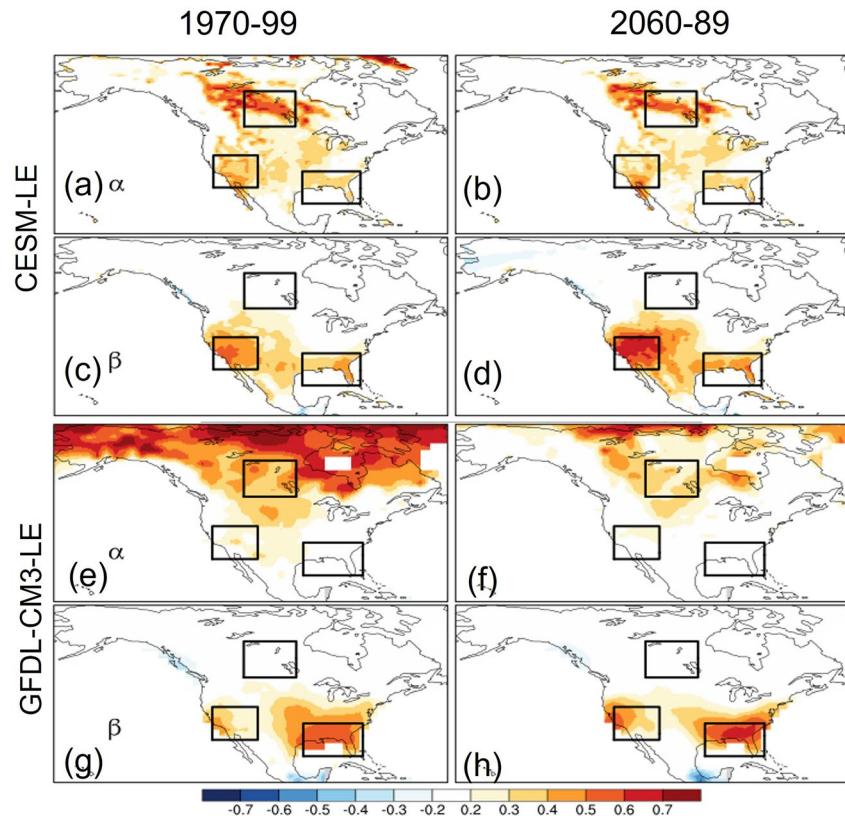
Figure 7. Drivers of changing hydroclimate variability and predictability. The figure shows α and β coefficients of the Reddened El Niño-Southern Oscillation (ENSO) framework model (Equation 1), where α represents the memory effect, and β represents the ENSO effect. Notice the weakening of α and strengthening of β, generally with global warming.

3.3.1. Multidecadal Modulations in Hydroclimate Predictability

Does hydroclimate predictability change from one 30-year climate period to another? We assessed the hydroclimate predictability in the five 30-year climate periods using the Reddened ENSO framework (Figure 8). Additionally, we diagnosed changes in the ENSO and Memory contributions to the hydroclimate predictability using the individual component-only model as discussed earlier (Figures 5c and 5d).

In the CESM-LE projections, the predictive skill of the ENSO model increased from 0.55 ± 0.03 in the 1940–1969 climate to 0.65 ± 0.05 in the 2060–2089 climate for the Southwest United States, and the corresponding improvement in the Southeast United States is 0.40 ± 0.03 to 0.60 ± 0.05 (cyan bars in Figures 8a and 8c). On the other hand, the Memory model shows a slight decline in predictive skill, from 0.36 ± 0.01 to 0.31 ± 0.01 in the Southwest United States and 0.25 ± 0.01 to 0.24 ± 0.01 in the Southeast United States (green bars in Figures 8a and 8c). However, the Reddened ENSO model shows improvement in the predictive skill from 0.66 ± 0.03 to 0.75 ± 0.05 in the Southwest United States and 0.53 ± 0.03 to 0.67 ± 0.05 in the Southeast United States (blue bars in Figures 8a and 8c). Hence, we attribute the improvement in the hydroclimate predictability to the increased ENSO effects.

The GFDL-CM3-LE model does not show a monotonic increase in ENSO-driven hydroclimate predictability, which can be related to the decadal modulation in ENSO variability changes (Figure 2b). For example, GFDL-CM3-LE showed the highest ENSO predictive skill (0.70 ± 0.03) in the Southeast United States during the 2000–2029 climate period, and the ENSO predictive skill declined to 0.61 ± 0.01 in the 2060–2089 period (cyan bars in Figure 8d); the ENSO variability also declined during the same period (Figure 2b). The GFDL-CM3-LE
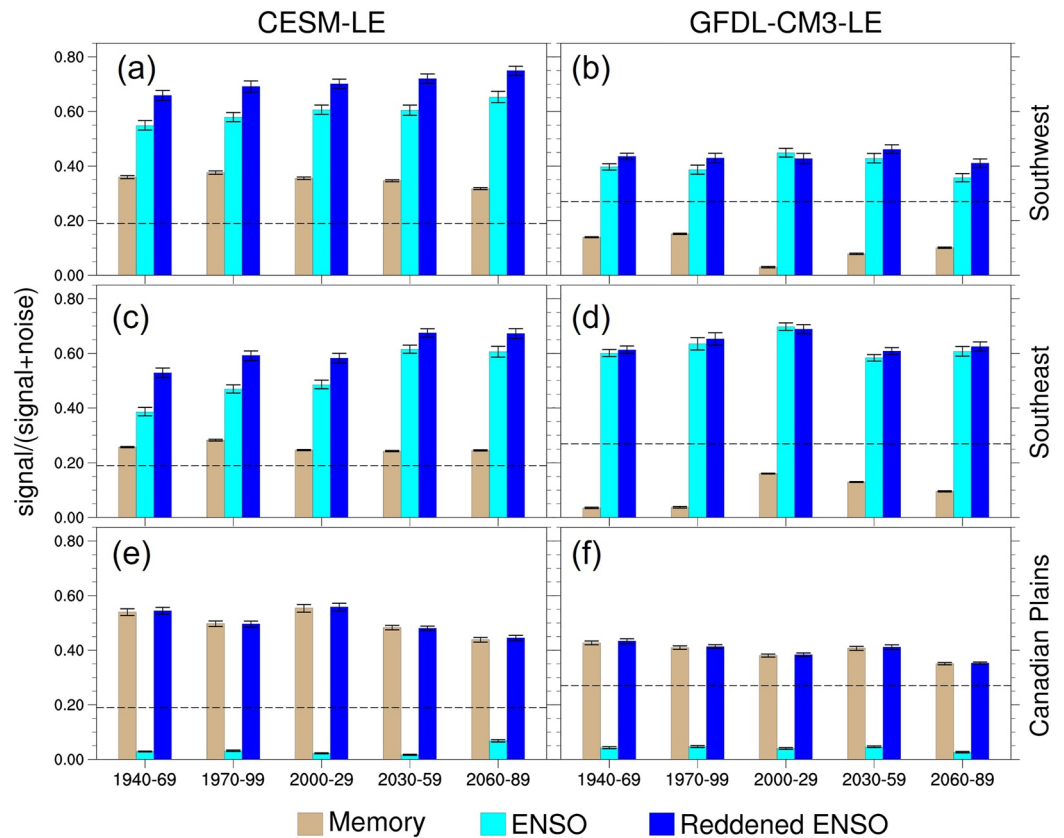
Figure 8. Multi-decadal modulation and changes in hydroclimate predictability. The bar plots show the evolution of signal-to-total ratios for the Memory + El Niño-Southern Oscillation (ENSO) model (Reddened ENSO) and compare them with the Memory only and ENSO only model in each of the three regions indicated by boxes on the maps in the previous figure. Error bars were determined by bootstrapping the signal-to-noise computation with 1,000 iterations with replacement. The dashed horizontal line shows the statistical significance at a 95% confidence level. Due to its smaller sample size (20), the GFDL-CM3-LE has a higher significance level than the CESM-LE (40).

projections show statistically insignificant contributions of the Memory model in the Southeast United States and Southeast (green bars in Figures 8b and 8d).

Due to a decreasing soil moisture memory effect, hydroclimate predictability can decline in high-latitude regions. For example, in the Canadian Plains, the CESM-LE projections show a decline in Memory model predictive skill from 0.54 ± 0.03 in the 1940–1969 climate to 0.44 ± 0.02 in the 2060–2089 climate (green bars in Figure 8e). The corresponding decline in the GFDL-CM3-LE projection is from 0.43 ± 0.01 to 0.35 ± 0.01 (green bars in Figure 8f). ENSO does not contribute significantly to the Canadian Plains' predictive skill in both climate models. Hence, total predictive skill (Reddened ENSO model) declined in the Canadian Plains (blue bars in Figures 8e and 8f).

3.3.2. Global Warming Reduces Soil Moisture Memory, Which Is Also Affected by Internal Climate Variability

The reduction in the memory contribution is generally consistent with the corresponding reduction in soil moisture memory time scale. However, inter-ensemble uncertainty is very large, leading to statistically insignificant changes in most mid-latitude regions of North America (Figure 9). In the 2060–2089 climate, the soil moisture memory decreases by $-9.9 \pm 12.8\%$, $-6.0 \pm 14.2\%$, and $-8.5 \pm 14.3\%$ in CESM-LE projections for the Southwest United States, and Southeast, and Canadian Plains, respectively. The corresponding reduction in GFDL-CM3-LE projections are: $-3.8 \pm 20.5\%$, $-1.1 \pm 17.3\%$, and $-11.9 \pm 22.4\%$. The GFDL-CM3-LE projections also show spatially adjacent positive and negative changes, for example, the northern part of the Southwest and the Western part of the Canadian Plains. Although, regions of increasing soil moisture memory are mostly statistically
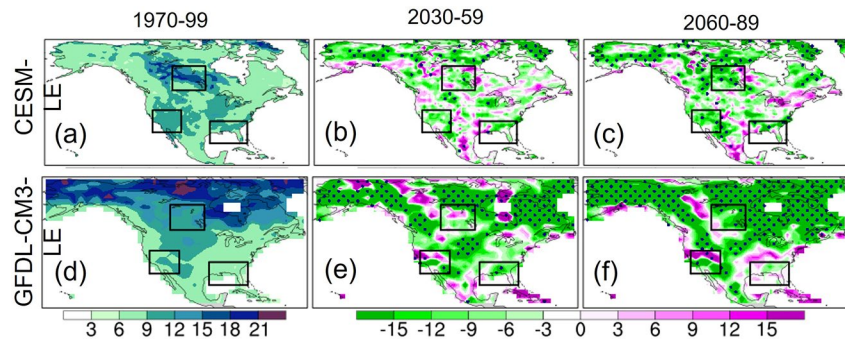
Figure 9. Soil moisture memory time scale projections in two large ensemble data. The left column shows the ensemble mean soil moisture memory (in months) in the 1970–1999 climate. The middle and right columns show the projected change in soil moisture memory in % compared to the 1970–1999 climate and for 2030–2059 and 2060–2089 projections. Notice a decrease in soil moisture memory in the future climate. Stipplings show statistical significance using the t test.

insignificant (Figures 9e and 9f) and could represent greater uncertainty in GFDL-CM3-LE memory projections due to the smaller ensemble size (=20 in GFDL-CM3-LE).

Increasing PET is a robust response to global warming in both large ensembles (Figure 10). For example, in Canadian Plains and CESM-LE projections, PET increases by $25.7 \pm 0.4\%$, and soil moisture memory decreases by $-10.5 \pm 4.1\%$; the corresponding changes in the GFDL-CM3-LE projections are $25.7 \pm 0.4\%$, and $-13.0 \pm 4.4\%$ respectively. Spatially averaged indices show a smaller inter-ensemble uncertainty than the local grid point average results discussed in the last paragraph. In the Southwest United States, the GFDL-CM3-LE projects a stronger PET increase ($23.4 \pm 0.3\%$) than CESM-LE ($15.2 \pm 0.2\%$). Note that GFDL-CM3-LE projects a much drier Southwest United States because of the projected precipitation decrease (Figure S6 in Supporting Information S1). GFDL-CM3-LE projections also show a multidecadal modulation in the soil moisture memory where the model shows a smaller change in the 2060–2089 period ($-6.5 \pm 8.5\%$) than in the 2000–2029 period ($-12.8 \pm 6.1\%$). The multidecadal modulation in soil moisture memory is generally the opposite sign of ENSO variability (Figure 2), that is, if ENSO variability decreases, then soil moisture memory increases and vice-versa. A similar multidecadal modulation in soil moisture memory changes is also found in the Southeast United States, where ENSO influence is stronger. Therefore, the soil moisture memory metric represents a coupled climate system response rather than land-only characteristics.

In summary, hydroclimate variability and predictability can change under the influence of ENSO and soil moisture memory effects. The ENSO effects become stronger, at least in CESM-LE projections, whereas soil moisture memory's effect becomes weaker under the global warming scenario. Next, we investigate their implications on hydroclimate climate extremes, including drought and pluvial risk.

3.4. Implications on Hydroclimate Extremes and Hydrologic Design

3.4.1. Power Spectra of Soil Moisture Variability

A decreasing soil moisture memory (Figure 9) can lessen the redness in the soil moisture variability spectra, which is further impacted by increasing ENSO variability (Figure 2); therefore, significant consequences for long-term droughts and pluvial conditions, for example, megadrought events. To explore this issue robustly, we used the Reddened ENSO framework to generate 1,000 synthetic soil moisture anomalies for every 30 years and the climate model ensemble (Section T1: Data Processing in Supporting Information S1). We compared the synthetic soil moisture power spectra with the corresponding climate models' power spectra with a limited sample size: 40 for CESM-LE and 20 for GFDL-CM3-LE. Finally, we bootstrapped the climate model's ensemble 1,000 times for comparison purposes and showed its median value in Figure 11.

Additionally, we compared the power spectra of the observed soil moisture variability (black line in Figure 11) with the large ensemble climate data for the historical period (blue line in Figure 11). We used ERA5-Land soil moisture data and observed SST data from 1950 to 2021 (*c.f.*, Figure 4).
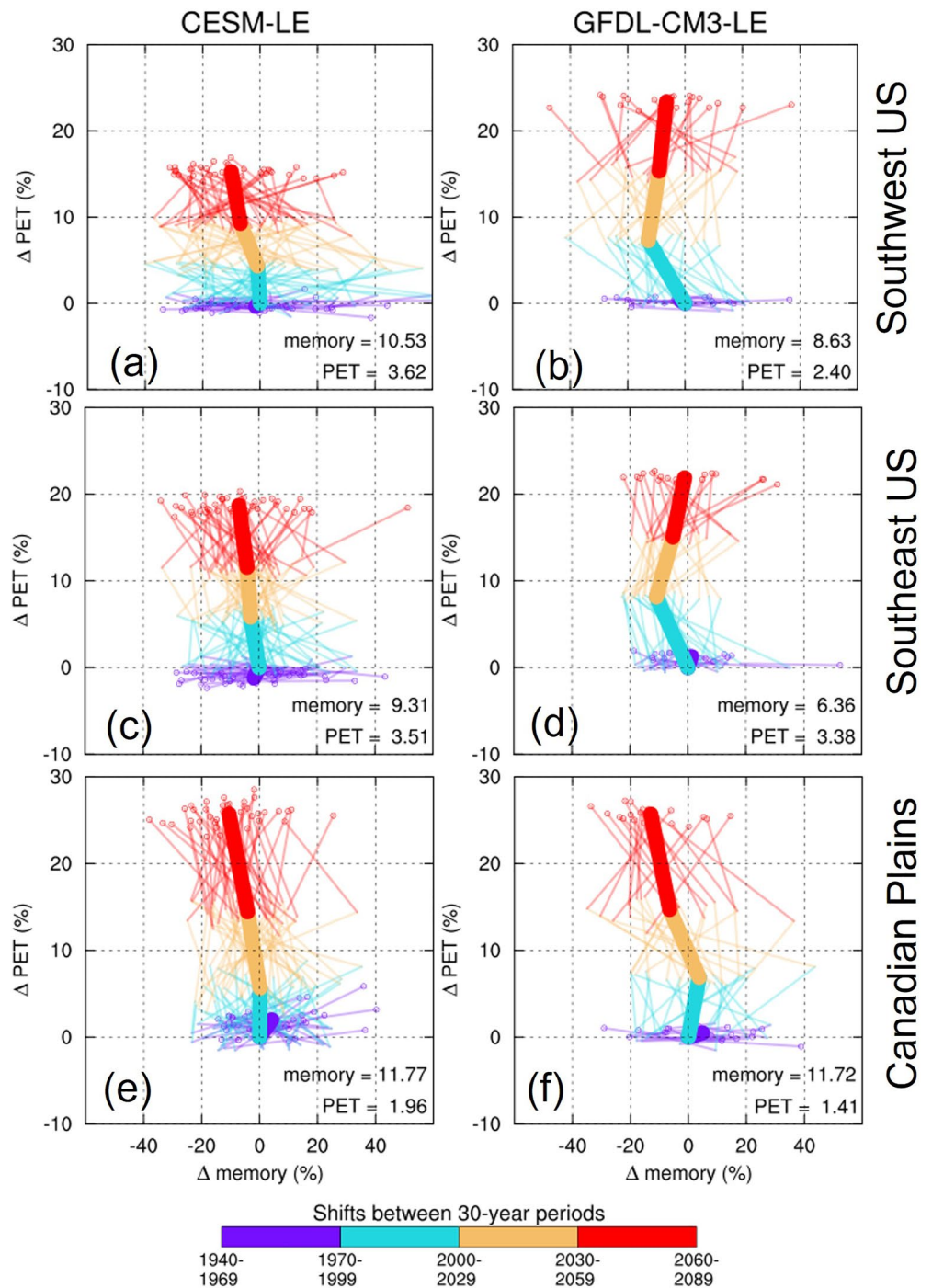
Figure 10. Increasing atmospheric water demand, decreasing soil moisture memory, and modulation related to El Niño-Southern Oscillation (ENSO) variability (see text). Same as Figure 2, the line scatters plot shows changes in potential evapotranspiration, soil moisture memory for individual ensembles (thin line), ensemble mean (thick line), and five climate periods relative to the 1970–1999 climate. Notice the decadal modulation in the soil moisture memory, especially in GFDL-CM3-LE projections for the Southwest and Southeast United States and compare it with the decadal modulation in ENSO changes (Figure 2).

We selected 100 random initial years between 1950 and 1992 and subsequent 30-year segments of soil moisture and ENSO. Next, we developed the synthetic power spectra using the Reddened ENSO framework (Equation 1), observation-based estimates of α, β, and ε as discussed previously (*c.f.*, Figure 5), and 30-year ENSO segments for the given observation ensemble. Using data only for the 1970–1999 period results in very large uncertainty
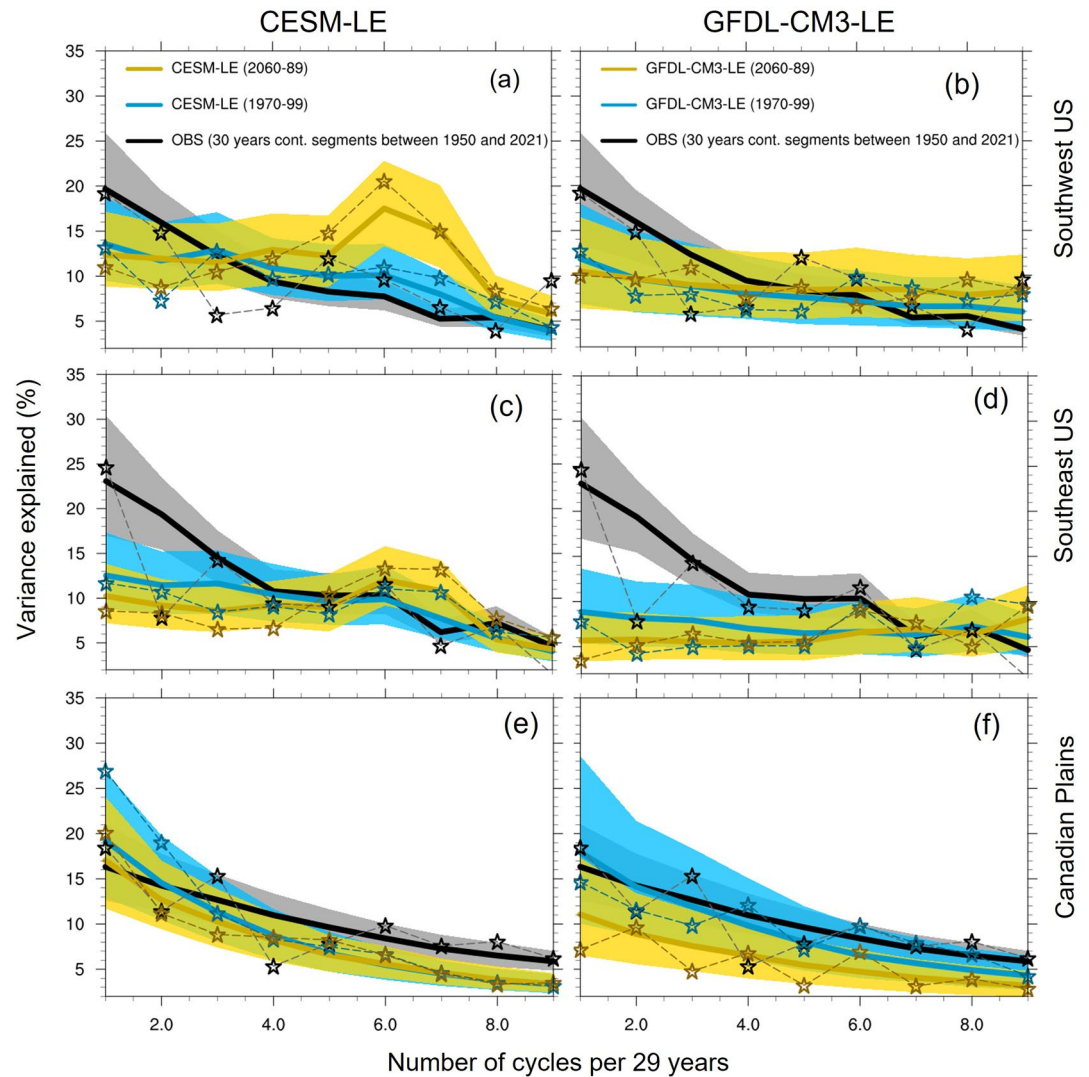
Figure 11. Power spectra of the soil moisture variability in observations and climate model projections. The figure shows the power spectra of the 1,000 samples of synthetic soil moisture anomalies. Their median and 95% uncertainty ranges are shown using solid lines and color shading. A dashed line with star markers shows the power spectra computed directly from the respective large ensemble data, mostly within the 95% uncertainty range of the synthetic data. The observation-based power spectra are developed using ERA5 soil moisture data, and Berkley Earth's SST data for El Niño-Southern Oscillation (ENSO) index from 1950 to 2021. Thirty-years continuous (cont.) segments of soil moisture and ENSO observations are randomly selected 100 times from the observations to make it comparable to climate models' historical power spectra. Notice (a) an underestimation of low-frequency variability in the climate models for Southwest United States, and Southeast, and (b) strengthening of the ENSO-related frequency's power (6–7 cycles per 29 years) in the CESM-LE future climate for the Southwest and Southeast United States.

in the observation-based power spectra due to its limited sample size (Figures S7 and S8 in Supporting Information S1). Further, it is assumed that changes in soil moisture and ENSO variability are relatively small during the historical period from 1950 to 2021 (cf. Figures 4b and 4c); hence using the entire observation period and sub-sample the 30-year continuous segments to create a large ensemble of the observation equivalent is justified.

Both climate models, CESM-LE and GFDL-CM3-LE, underestimate low-frequency soil moisture variability (1–3 cycles per 29 years) compared to observation in the Southwest and Southeast United States (Figures 11a–11d). For example, in the Southwest United States and the observation-based synthetic power spectra, the lowest frequency (frequency 1) explains 19.6% of the total variance (range: 13.4%–25.9%), compared to 13.6% in CESM-LE (range: 9.5%–18.7%), and 11.8% in GFDL-CM3-LE historical data (range:

6.8%–18.0%). The underestimation of low-frequency hydroclimate variability is a known issue in climate models (Ault et al., 2013; Cheung et al., 2017; Kumar et al., 2013; Pierce et al., 2022). Additionally, the observation-based synthetic power spectra have uncertainty due to their limited sample size (72 years of data), as some of the resampled observations fall outside the 95% range of the synthetic power spectra, for example, frequencies 3 and 4 in the Southwest United States, and frequency 2 in the Southeast United States (see dashed line in Figure 11). The observation-based power spectra generally overlap with climate models' power spectra in the Canadian Plains.

The synthetic soil moisture power spectra generated using the large ensemble climate data capture the corresponding climate models' power spectra within the 95% range uncertainty estimate of the synthetic model (Figure 11). In fact, synthetic power spectra show a smooth transition from one frequency to the subsequent frequency. In contrast, the climate model's ensemble can show a zig-zag pattern, for example, a lower frequency spectrum (1–3 cycles in 29 years) in the Southwest United States and CESM-LE projections. Hence, we argue that a very large sample size is needed to investigate power spectra, and the synthetic model approach is helpful.

The CESM-LE synthetic spectra show an increase in the power for ENSO-related frequency (6–7 cycles per 29 years) in the 2060–2089 climate compared to the 1970–1999 climate and in the Southwest United States. For example, the power of the 6 cycles per 29 years frequency increased from 10.1% (range: 7.5%–13.6%) in the historical climate to 17.5% (range: 13.3%–22.8%) in the future. The Southeast United States projections show a minor increase in the power from 10% (range: 7.0%–13.6%) to 12.0% range (9.2%–15.8%) for the ENSO-related frequency. On the other hand, in the Canadian Plains, the spectral power decreased across all frequencies, especially in the GFDL-CM3-LE future projections, due to an overall decreased soil moisture variability (Figure 3f). However, the lower frequency power decreased more than the higher frequency. For example, the spectral power of frequency 1 decreased from 17.9% (range: 10.0%–28.6%) to 11.1% (range: 6.5 to 17.3), and frequency 6 decreased from 6.5% (range: 4.0%–9.7%) to 4.7% (range: 2.9%–7.1%).

The GFDL-CM3-LE synthetic power spectra are relatively white, that is, low frequency has similar power as the high-frequency in the Southwest and Southeast United States (Figures 11b and 11d). This can be expected due to the minor role of memory in GFDL-CM3-LE projections (Figures 8b and 8d). Nonetheless, this comparison provides an important insight into how soil moisture memory contributes to the redness in the spectrum, and if soil moisture memory is absent, then the spectrum can look white, as demonstrated next.

The soil moisture memory effects contribute to the redness in hydroclimate (soil moisture) variability spectra, demonstrated using counterfactual analysis, that is, removing the soil moisture memory effects in the Reddened ENSO framework. Figure 12 shows the soil moisture variability spectra using the ENSO-only model in the Southwest and Southeast United States, where the ENSO-only model shows statistically significant prediction skill (Figure 5c, and cyan bars in Figures 8a–8d). To remind the reader, redness is the increase in spectral power with lower frequencies. The redness has disappeared in the ENSO-only model (Figure 12), highlighting the advantage of developing a simpler model (the Reddened ENSO framework) to understand the changing hydroclimate variability and predictability. In the Southwest United States, the ENSO effects are relatively stronger in CESM-LE than in GFDL-CM3-LE, which is comparable to the observations (Figures 12a and 12b).

3.4.2. Implications for Drought and Pluvial Risks

The hydroclimate extreme analysis is often less robust due to the small sample size, for example, one in a 100-year event has only one sample in 100 years of simulation or observation. We use the Reddened ENSO framework (Equation 1) to augment the sample size to 1,000 for a robust assessment of the drought and pluvial risks (see Section T1: Data Processing in Supporting Information S1). Additionally, we separate the contributions of mean and variances for each climate model's October–September mean soil moisture anomalies generated by the Reddened ENSO model. October–September is defined as the water year by the United States Geological Survey. First, the Reddened ENSO model (Equation 1) derived synthetic anomalies after removing the trend (*detrended*) represented by S_t in Equation 1, that is, taking out ensemble mean anomalies in the respective large ensemble data set, keeping the variance the same as in the projected climate, and isolating the variance's contribution only.
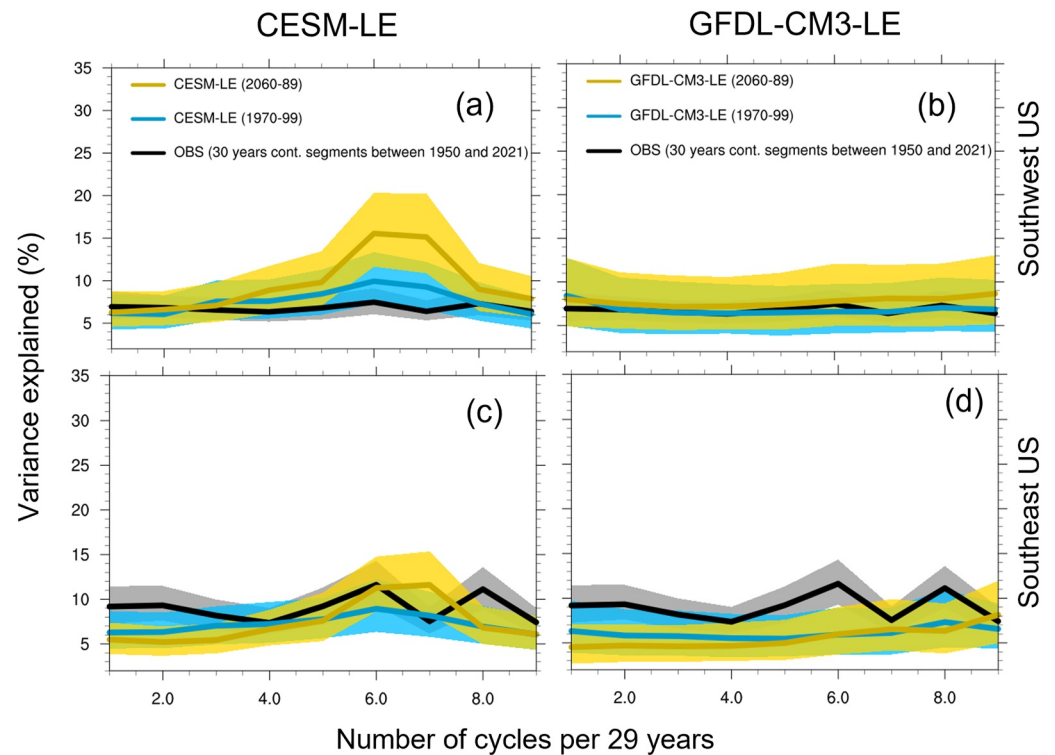
Figure 12. Soil moisture power spectra using El Niño-Southern Oscillation (ENSO)-only model. Same as Figure 11 using ENSO-only model. Notice the disappearance of the redness in the power spectra (see text).

We also derived synthetic anomalies with respect to the historical climatology (*with trend*), therefore providing the contribution of *mean + variance* changes in future hydroclimate extremes as follows:

$$S_{(t)}^{wt} = \Delta s_{GW} + \alpha\, S_{(t-1)} + \beta\, E_{(t)} + \varepsilon \tag{6}$$

Where Δs_{GW} is the global warming signal computed as the large ensemble mean soil moisture anomalies relative to the 1970–1999 climate in the respective climate model.

Changes in the mean soil moisture due to global warming drive shifts in the drought and pluvial distribution (Figure 13). We define a drought (pluvial) event as occurring when soil moisture anomalies are below (above) zero, with event *duration* defined as the number of consecutive years of the same sign and event *severity* measured by the magnitude of anomalies summed over the entire event (see inset in Figure 13). The exceedance probabilities of droughts and pluvial are determined as follows: (a) identify droughts and pluvial events in each 40×30 (20×30) years segments of the CESM-LE (GFDL-CM3-LE) of the LE data or the corresponding synthetic soil moisture anomalies. (b) Rank the events as per their severity or duration and compute the probability distribution of the ranked events. In the 2060–2089 period, drought severity is rescaled to its standard deviation in the reference climate period, that is, 1970–1999. Exceedance probability is one minus cumulative probability. (c) Thus, 1,000 synthetic samples of the droughts or pluvial distribution are obtained, and their 95% ranges and median values are shown in Figure 13. For comparison, we bootstrapped the LE data with replacement 1,000 times, and its median values are also shown in Figure 13.

Figure 13 shows the drought and pluvial risk comparison between historical and future climates using two large ensemble climate data and corresponding synthetic models. A comparison with observations in the historical climate is shown in the supplementary (Figure S9 in Supporting Information S1) because of two main reasons: (a) the synthetic model can be reliably estimated using the large ensemble climate data (cf., Figure 11), and (b) the main goal is to understand future changes which are only available from the large ensemble data. Both large ensembles generally produce drought and pluvial risk comparable to the observations (Figure S7 in Supporting Information S1). Biases are with ±50% for 20 out of 24 cumulative distribution curves (Figure S7 in Supporting
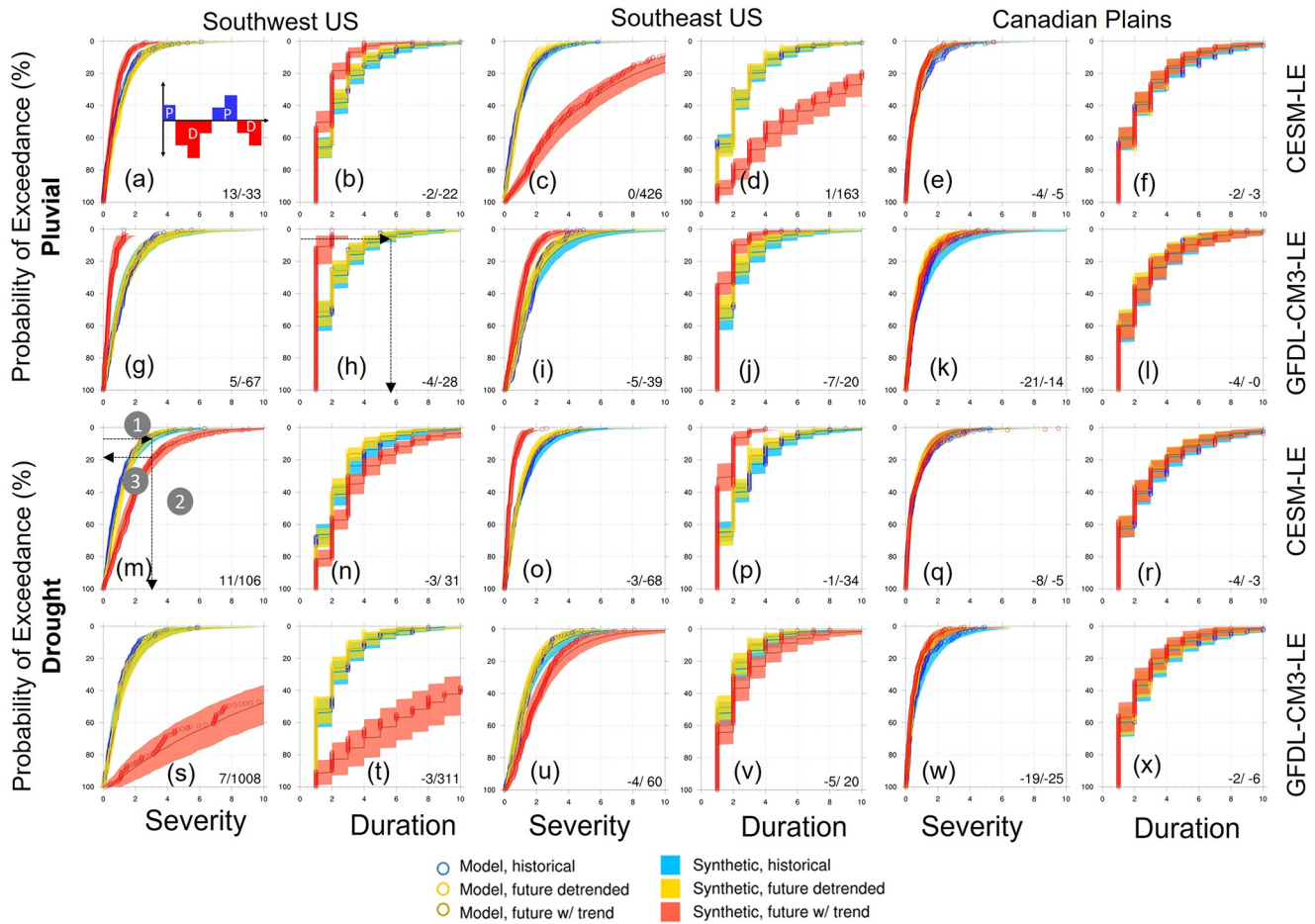
Figure 13. Changing drought and pluvial risk—the role of mean and variability changes. Severity and duration of drought and pluvial events in synthetic soil moisture anomalies generated from Reddened El Niño-Southern Oscillation (ENSO) model (Equation 1, color shading) and respective large ensemble data star symbols. Empirical cumulative distribution functions for severity (left column) and duration (right column) of drought (flood) events, defined here as a consecutive 12-month running mean soil moisture anomalies below (above) 0. Duration is given in the number of years, and severity is obtained by accumulating the absolute value of the anomalies throughout the duration of the event. The blue curves are representative of 1970–1999, the red curves represent 2060–2089, and the orange curves represent future "*detrended*" time series. The number in each panel xx/yy represents the total shift in the detrended/and trend distributions compared to the historical climate. Notice that changes are significant only when mean change (with trend) is included in the distribution. Inset figure (a): D—drought, P—pluvial.

Information S1). Both models underestimate pluvial durations in the Southeast (−62% for CESM-LE, and −84% in GFDL-CM3-LE) and drought severity in the Southwest (−43% in CESM-LE, and −26% in GFDL-CM3-LE), consistent with the corresponding power spectra analysis (Figure 11). Nonetheless, the observational analysis provides an uncertainty context (±50%) to assess robustness in future projections.

The synthetic soil moisture anomalies reliably produce the distribution of the droughts and pluvial events as found in the corresponding LE data, that is, they are found within the 95% range of the synthetic distributions as shown in color shading in Figure 13. For example, in the Southwest United States for the CESM-LE model, the value of the 5% exceedance probability drought severity increased from 3.1 accumulated standard deviations in the historical period (1970–1999) to 6.2 in the future period with the trend (2060–2089), while the corresponding values from the synthetic soil moisture anomalies were 3.3 (range: 2.8–4.0) and 5.5 (range: 4.6–6.7), respectively. Additionally, the synthetic anomalies give the distribution a better smooth fit than the original bootstrapped data (compare the solid line with the corresponding color markers in Figure 13). Therefore, the Reddened ENSO framework can also be seen as a physically interpretable distribution function where model parameters can be reliably estimated from the climate model outputs or observations. Hereafter, we discuss the synthetical anomalies results and refer to them as the robust projections

from the CESM-LE and GFDL-CM3-LE because the synthetic model parameters were estimated from the respective climate models.

Future "*detrended*" hydroclimate extremes almost overlap with their historical distribution, as can be seen by comparing the yellow shading curve with the blue shading in Figure 13. In other words, if we recenter the future distribution by removing its new mean climate, then future drought and pluvial risk may look like the historical climate. Changes in the drought and pluvial risks are considerably more minor in the detrended future climate than with the trend. For example, in the Southwest United States and GFDL-CM3-LE projections, drought severity risk increases by 7% in the detrended future climate compared to a 1,008% increase in the future climate with the trend. Numbers represent a % increase in the area left to the median line relative to the historical climate (Figure 13).

The mean climate change (with trend) introduces considerable shifts in the drought and pluvial distributions for the Southeast and Southwest United States (Figure 13). A shift to the right means more severe and more prolonged droughts, and the opposite is for a left shift in the distribution. Both climate models project more severe and prolonged drought in the Southwest United States while the pluvial risk lessens. The projected drought risk is considerably higher in GFDL-CM3-LE projections than the CESM-LE projections for the Southwest United States. For example, GFDL-CM3-LE projects a 1,008% increased drought severity risk compared to 106% in the CESM-LE projections. An increase in drought duration is generally proportional to the drought severity increases, that is, if severity increases, then duration also increases. However, the magnitude of the drought duration increase is generally smaller than the drought severity. For example, the GFDL-CM3-LE projections show a 311% increase in drought duration in the Southwest United States (Figures 13s and 13t).

Climate model projections differ in the Southeast United States, where CESM-LE projects increased pluvial severity (426%) and decreased drought severity (−68%). Opposite results are found in the GFDL-CM3-LE projections, which show a slightly decreased pluvial severity (−39%) and an increased drought severity (60%).

In the Canadian Plains, both climate models show minimal changes in drought and pluvial risks consistent with minimal changes in mean soil moisture (Figures 3e and 3f). This result again emphasizes that the mean state changes mainly drive the future drought and pluvial risks despite uncertainty in the variability projections.

3.4.3. Implications for Hydrologic Design

A 5% exceedance probability event is critical in hydrologic design (Chow et al., 1988). Therefore, we have assessed projected change in the 5% exceedance probability event as found in the historical climate. Figure 13*m* illustrates the example: the 5% exceedance probability event in the CESM-LE historical climate has a drought severity of 3.1 accumulated standard deviations, and a similar magnitude event in the future climate with a trend has the exceedance probability of 22% (range: 17%–27%).

Figure 14 shows the projected change in the 5% exceedance probability events with and without trend and in reference to the historical climate. Consistent with the earlier discussion, the exceedance probability of the "*detrended*" future climate is not considerably different from the historical climate. However, it changes considerably when the trend is included. Some notable changes are the GFDL-CM3-LE projects that a 5% exceedance probability drought severity event can become much more frequent in the Southwest United States with a median exceedance probability of 79% (range: 68%–90%). On the other hand, pluvial extremes can become less frequent and shorter in the Southwest United States. In fact, the GFDL-CM3-LE projection does not find any pluvial event that lasts for 5 years which is the pluvial duration of the 5% exceedance probability event in the historical climate (see Figure 13h).

The divergent response is found in the Southeast United States, where a 5% exceedance probability pluvial severity event becomes more frequent with a median frequency of 56% (range: 48%–64%) in CESM-LE projections and less frequent in GFDL-CM3-LE projections with a median frequency of 1% (range: 1%–3%). Similarly, a 5% exceedance probability drought severity event becomes less frequent with a median frequency of 1% (range: 0.8%–1.1%) in CESM-LE projections and more frequent in GFDL-CM3-LE projections with a median frequency of 19.3% (range: 12.7%–25.9%). We did not analyze the 5% exceedance probability event for the Canadian Plains because they show minimal changes (two rightmost columns in Figure 13).
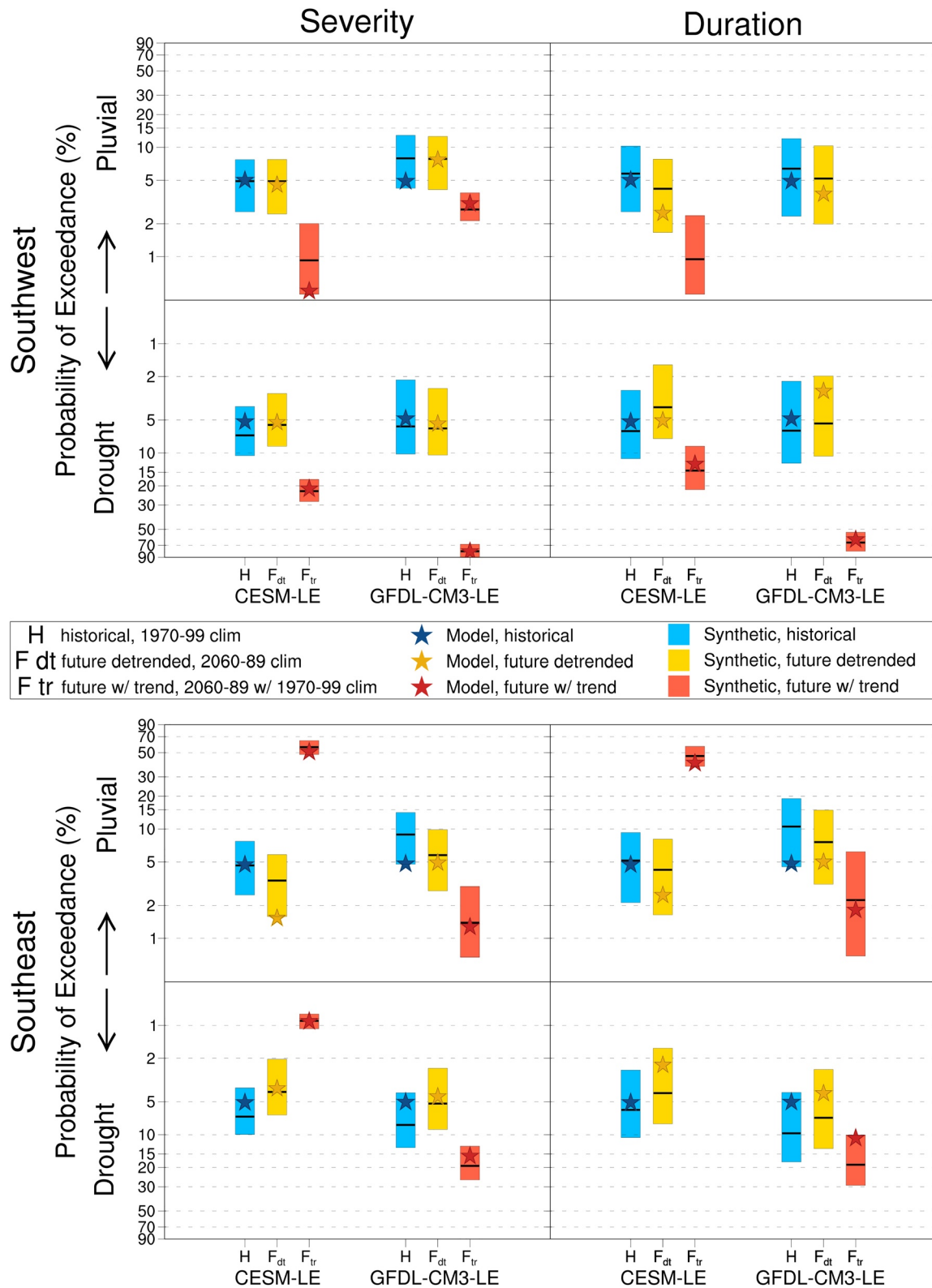
Figure 14.

4. Discussion and Conclusions

A smaller change in land hydroclimate variability can be attributed to the decreasing soil moisture memory effects under global warming scenarios (e.g., Figures 9 and 10). Soil moisture variability is directly proportional to the memory effects, that is, a higher memory can contribute to more variability and vice versa (Equation 1). Hydroclimatic time series with long-term memory (persistence) show higher variability than less or no memory time series (Hamed, 2008; Koutsoyiannis, 2003). In addition, soil moisture memory (persistence) increases with soil depth (Mishra et al., 2015), so changes in soil moisture variability can be sensitive to soil depths. In parallel research, Shi et al. (2022) found a reduction in the upper-layer ocean memory due to global warming in the CMIP6 climate model's projections.

Konapala et al. (2020) found a reduction in seasonal evapotranspiration variability despite increased precipitation variability due to global warming. Evapotranspiration is another metric for land hydroclimate variability. Hence, a reduction or smaller change in soil moisture variability is consistent with the findings reported by Konapala et al. (2020).

Contrastingly, increasing ENSO and precipitation variability (Figures 1 and 2) can increase soil moisture variability (Equation 1). The ENSO variability projections are considerably uncertain in climate models (Beobide-Arsuaga et al., 2021). The two climate models selected in this study, CESM-LE and GFDL-CM3-LE, projected increased ENSO variability, which is generally consistent with other large ensemble climate data (Maher et al., 2018; Rodgers et al., 2021).

Effects of soil moisture memory on hydroclimate predictability are generally smaller in GFDL-CM3-LE than CESM-LE, especially in the mid-latitude regions (Figure 8). Kumar et al. (2019) found a similar soil moisture memory between Community Land Model and Noah Land Surface Model; respective climate model's land component driven by the observed meteorological forcing. CESM-LE shows a stronger correlation between total water storage anomalies and hydroclimate variability in the subsequent growing season than satellite-based observations and GFDL climate models (Levine et al., 2016). ENSO teleconnection strength is stronger in CESM-LE data than GFDL-CM3-LE, especially in the Southwest United States (e.g., Figures 8a and 8b). Future studies can explore inter-model differences using the new generation of large ensemble climate data (e.g., Delworth et al., 2020; Rodgers et al., 2021).

For both models and observations, the Reddened ENSO framework provides a useful null hypothesis to evaluate changing land hydroclimate variability and predictability in North America. The Reddened ENSO framework shows comparable performance to the dynamical prediction system for predicting year-to-year soil moisture variations (e.g., Figure 5). Using the Reddened ENSO framework, we find that increasing ENSO-teleconnected precipitation variability and decreasing land memory could offset, resulting in little net change in land hydroclimate variability. However, these changes would also lead to increased (decreased) land hydroclimate variability on annual (decadal) time scales (cf. Figure 11).

Despite uncertainty in the variability projections, the soil moisture mean state changes can drive future drought and pluvial risks at regional scales (e.g., Figures 13 and 14). The Reddened ENSO framework robustly demonstrated mean-state-driven changes in hydroclimate extremes using two large ensemble climate data and increasing their sample size to 1,000 (e.g., Figure 14), which is otherwise not feasible. The mean-state-driven changes can have important implications for long-term water planning. For example, Barnett and Pierce (2008) used mean-state-driven inflow changes and projected that Lake Mead is likely to dry (50% probability) by 2021, which appears to be the case today.

Figure 14. Projected changes in the probability of exceedance of wet and dry extremes over the Southwest (top panel) and the Southeast (bottom panel) in 2060–2089 relative to 1970–1999. Taking the 95th percentile event—which has a 5% probability of exceedance—from each model's (CESM-LE and GFDL-CM3-LE) historical (1970–1999) distributions of pluvials (top row in each panel) and droughts (bottom row in each panel), we quantify the projected changes in the probability of exceedance of events of equivalent severity (left column) and duration (right column). The stars denote probabilities given by each climate model's soil moisture anomalies, while bars denote the probabilities estimated with the synthetic soil moisture anomalies (the black horizontal line illustrating the median of said ranges). The blue stars/bars represent the historical 30-year period; the yellow stars/bars represent the future 30-year period where anomalies were computed relative to that period's climatology (in effect, removing the externally forced trend); the red stars/bars represent the same future 30-year period where anomalies were computed relative to the historical climatology (thereby including the trend).

Conflict of Interest

The authors declare no conflicts of interest relevant to this study.

Data Availability Statement

The CESM-LE and GFDL-CM3-LE data are freely available from the Multi-model Large Ensemble Archive (https://www.cesm.ucar.edu/projects/community-projects/MMLEA). The CESM-LE data are available directly on NCAR supercomputer (/glade/campaign/cesm/collections/cesmLE), also available through Amazon Web Services (AWS) S3 at https://doi.org/10.26024/wt24-5j82. GFDL-CM3-LE data are available through Climate Data Gateway: https://www.earthsystemgrid.org/dataset/ucar.cgd.ccsm4.CLIVAR_LE.gfdl_cm3_lens.html; also available directly on NCAR supercomputer:/glade/collections/cdg/data/CLIVAR_LE/gfdl_cm3_lens. SMYLE data are available through Climate Data Gateway: https://doi.org/10.26024/pwma-re41; also available at NCAR supercomputer:/glade/campaign/cesm/development/espwg/SMYLE/archive/. ERA5-Land data are available through ECMWF (https://www.ecmwf.int/en/forecasts/datasets/reanalysis-datasets/era5). Berkeley Earth Data are available from https://berkeleyearth.org/data/; we used 1° gridded data Monthly Land + Ocean, Average Temperature with Air Temperature at Sea Ice (1850 to Recent). Lake Mead, Water Level data, is available from the Bureau of Reclamation (https://www.usbr.gov/lc/region/g4000/hourly/mead-elv.html). All analysis scripts are available through GitHub repository that is open access: https://github.com/cwsauburn/NA_Hydroclimate. The GitHub repository is linked to Zenodo, a FAIR compliant repository https://doi.org/10.5281/zenodo.7686292.

References

Allan, R., Barlow, M., Byrne, M. P., Cherchi, A., Douville, H., Fowler, H. J., et al. (2020). Advances in understanding large-scale responses of the water cycle to climate change. *Annals of the New York Academy of Sciences*, *1472*(1), 49–75. https://doi.org/10.1111/nyas.14337

Allen, R. J., & Luptowitz, R. (2017). El Niño-like teleconnection increases California precipitation in response to warming. *Nature Communications*, *8*(1), 1–15. https://doi.org/10.1038/ncomms16055

Amenu, G. G., Kumar, P., & Liang, X. Z. (2005). Interannual variability of deep-layer hydrologic memory and mechanisms of its influence on surface energy fluxes. *Journal of Climate*, *18*(23), 5024–5045. https://doi.org/10.1175/jcli3590.1

Ault, T. R., Cole, J. E., Overpeck, J. T., Pederson, G. T., George, S. S., Otto-Bliesner, B., et al. (2013). The continuum of hydroclimate variability in western North America during the last millennium. *Journal of Climate*, *26*(16), 5863–5878. https://doi.org/10.1175/jcli-d-11-00732.1

Ault, T. R., George, S. S., Smerdon, J. E., Coats, S., Mankin, J. S., Carrillo, C. M., et al. (2018). A robust null hypothesis for the potential causes of megadrought in western North America. *Journal of Climate*, *31*(1), 3–24. https://doi.org/10.1175/jcli-d-17-0154.1

Barnett, T. P., & Pierce, D. W. (2008). When will Lake Mead go dry? *Water Resoures Research*, *44*(3), W03201. https://doi.org/10.1029/2007wr006704

Bellucci, A., Haarsma, R., Bellouin, N., Booth, B., Cagnazzo, C., van den Hurk, B., et al. (2015). Advancements in decadal climate predictability: The role of nonoceanic drivers. *Reviews of Geophysics*, *53*(2), 165–202. https://doi.org/10.1002/2014RG000473

Beobide-Arsuaga, G., Bayr, T., Reintges, A., & Latif, M. (2021). Uncertainty of ENSO-amplitude projections in CMIP5 and CMIP6 models. *Climate Dynamics*, *56*(11), 3875–3888. https://doi.org/10.1007/s00382-021-05673-4

Cheung, A. H., Mann, M. E., Steinman, B. A., Frankcombe, L. M., England, M. H., & Miller, S. K. (2017). Comparison of low-frequency internal climate variability in CMIP5 models and observations. *Journal of Climate*, *30*(12), 4763–4776. https://doi.org/10.1175/jcli-d-16-0712.1

Chikamoto, Y., Timmermann, A., Stevenson, S., DiNezio, P., & Langford, S. (2015). Decadal predictability of soil water, vegetation, and wildfire frequency over North America. *Climate Dynamics*, *45*(7–8), 2213–2235. https://doi.org/10.1007/s00382-015-2469-5

Chow, V. T., Maidment, D. R., & Mays, L. W. (1988). Applied hydrology.

Cook, B., Mankin, J., Marvel, K., Williams, A., Smerdon, J., & Anchukaitis, K. (2020). Twenty-first century drought projections in the CMIP6 forcing scenarios. *Earth's Future*, *8*(6), e2019EF001461. https://doi.org/10.1029/2019ef001461

Dai, A., Fyfe, J. C., Xie, S.-P., & Dai, X. (2015). Decadal modulation of global surface temperature by internal climate variability. *Nature Climate Change*, *5*(6), 555–559. https://doi.org/10.1038/nclimate2605

DelSole, T., Yan, X., Dirmeyer, P. A., Fennessy, M., & Altshuler, E. (2014). Changes in seasonal predictability due to global warming. *Journal of Climate*, *27*(1), 300–311. https://doi.org/10.1175/jcli-d-13-00026.1

Delworth, T. L., Cooke, W. F., Adcroft, A., Bushuk, M., Chen, J. H., Dunne, K. A., et al. (2020). SPEAR: The next generation GFDL modeling system for seasonal to multidecadal prediction and projection. *Journal of Advances in Modeling Earth Systems*, *12*(3), e2019MS001895. https://doi.org/10.1029/2019ms001895

Delworth, T. L., & Manabe, S. (1988). The influence of potential evaporation on the variabilities of simulated soil wetness and climate. *Journal of Climate*, *1*(5), 523–547. https://doi.org/10.1175/1520-0442(1988)001<0523:tiopeo>2.0.co;2

Deser, C., Lehner, F., Rodgers, K., Ault, T., Delworth, T., DiNezio, P., et al. (2020). Insights from Earth system model initial-condition large ensembles and future prospects. *Nature Climate Change*, *10*(4), 1–10. https://doi.org/10.1038/s41558-020-0731-2

Dewes, C. F., Rangwala, I., Barsugli, J. J., Hobbins, M. T., & Kumar, S. (2017). Drought risk assessment under climate change is sensitive to methodological choices for the estimation of evaporative demand. *PLoS One*, *12*(3), e0174045. https://doi.org/10.1371/journal.pone.0174045

Diffenbaugh, N. S., Swain, D. L., & Touma, D. (2015). Anthropogenic warming has increased drought risk in California. *Proceedings of the National Academy of Sciences of the United States of America*, *112*(13), 3931–3936. https://doi.org/10.1073/pnas.1422385112

Ding, H., Newman, M., Alexander, M. A., & Wittenberg, A. T. (2018). Skillful climate forecasts of the tropical Indo-Pacific Ocean using model-analogs. *Journal of Climate*, *31*(14), 5437–5459. https://doi.org/10.1175/jcli-d-17-0661.1

Esit, M., Kumar, S., Pandey, A., Lawrence, D. M., Rangwala, I., & Yeager, S. (2021). Seasonal to multi-year soil moisture drought forecasting. *npj Climate and Atmospheric Science*, *4*(1), 16. https://doi.org/10.1038/s41612-021-00172-z

Fasullo, J., Otto-Bliesner, B., & Stevenson, S. (2018). ENSO's changing influence on temperature, precipitation, and wildfire in a warming climate. *Geophysical Research Letters*, *45*(17), 9216–9225. https://doi.org/10.1029/2018gl079022

Frankignoul, C., & Hasselmann, K. (1977). Stochastic climate models, Part II Application to sea-surface temperature anomalies and thermocline variability. *Tellus*, *29*(4), 289–305. https://doi.org/10.1111/j.2153-3490.1977.tb00740.x

Gonzalez, P. L., & Goddard, L. (2016). Long-lead ENSO predictability from CMIP5 decadal hindcasts. *Climate Dynamics*, *46*(9–10), 3127–3147. https://doi.org/10.1007/s00382-015-2757-0

Guo, Z. C., Dirmeyer, P. A., & DelSole, T. (2011). Land surface impacts on subseasonal and seasonal predictability. *Geophysical Research Letters*, *38*(24), L24812. https://doi.org/10.1029/2011gl049945

Hamed, K. H. (2008). Trend detection in hydrologic data: The Mann–Kendall trend test under the scaling hypothesis. *Journal of Hydrology*, *349*(3–4), 350–363. https://doi.org/10.1016/j.jhydrol.2007.11.009

Ham, Y.-G., Kim, J.-H., & Luo, J.-J. (2019). Deep learning for multi-year ENSO forecasts. *Nature*, *573*(7775), 568–572. https://doi.org/10.1038/s41586-019-1559-7

Hasselmann, K. (1976). Stochastic climate models. Part 1. Theory. *Tellus*, *28*(6), 473–485. https://doi.org/10.1111/j.2153-3490.1976.tb00696.x

Hurst, H. E. (1951). Long-term storage capacity of reservoirs. *Transactions of the American Society of Civil Engineers*, *116*(1), 770–799. https://doi.org/10.1061/taceat.0006518

Kam, J., & Sheffield, J. (2016). Increased drought and pluvial risk over California due to changing oceanic conditions. *Journal of Climate*, *29*(22), 8269–8279. https://doi.org/10.1175/Jcli-D-15-0879.1

Kay, J. E., Deser, C., Phillips, A., Mai, A., Hannay, C., Strand, G., et al. (2015). The Community Earth System Model (CESM) large ensemble project a community resource for studying climate change in the presence of internal climate variability. *Bulletin of the American Meteorological Society*, *96*(8), 1333–1349. https://doi.org/10.1175/bams-d-13-00255.1

Konapala, G., Mishra, A. K., Wada, Y., & Mann, M. E. (2020). Climate change will affect global water availability through compounding changes in seasonal precipitation and evaporation. *Nature Communications*, *11*(1), 1–10. https://doi.org/10.1038/s41467-020-16757-w

Koutsoyiannis, D. (2003). Climate change, the Hurst phenomenon, and hydrological statistics. *Hydrological Sciences Journal*, *48*(1), 3–24. https://doi.org/10.1623/hysj.48.1.3.43481

Kumar, S., Dirmeyer, P. A., & Kinter, J. (2014). Usefulness of ensemble forecasts from NCEP Climate Forecast System in sub-seasonal to intra-annual forecasting. *Geophysical Research Letters*, *41*(10), 3586–3593. https://doi.org/10.1002/2014gl059586

Kumar, S., Kinter, J., Dirmeyer, P. A., Pan, Z. T., & Adams, J. (2013). Multidecadal climate variability and the "warming hole" in North America: Results from CMIP5 twentieth- and twenty-first-century climate simulations. *Journal of Climate*, *26*(11), 3511–3527. https://doi.org/10.1175/Jcli-D-12-00535.1

Kumar, S., Newman, M., Lawrence, D. M., Lo, M.-H., Akula, S., Lan, C.-W., et al. (2020). The GLACE-hydrology experiment: Effects of land-atmosphere coupling on soil moisture variability and predictability. *Journal of Climate*, *33*(15), 6511–6529. https://doi.org/10.1175/JCLI-D-19-0598.1

Kumar, S., Newman, M., Wang, Y., & Livneh, B. (2019). Potential reemergence of seasonal soil moisture anomalies in North America. *Journal of Climate*, *32*(10), 2707–2734. https://doi.org/10.1175/jcli-d-18-0540.1

Kumar, S., Zwiers, F., Dirmeyer, P. A., Lawrence, D. M., Shrestha, R., & Werner, A. T. (2016). Terrestrial contribution to the heterogeneity in hydrological changes under global warming. *Water Resources Research*, *52*(4), 3127–3142. https://doi.org/10.1002/2016wr018607

Levine, P. A., Randerson, J. T., Swenson, S. C., & Lawrence, D. M. (2016). Evaluating the strength of the land–atmosphere moisture feedback in Earth system models using satellite observations. *Hydrology and Earth System Sciences*, *20*(12), 4837–4856. https://doi.org/10.5194/hess-20-4837-2016

Maher, N., Matei, D., Milinski, S., & Marotzke, J. (2018). ENSO change in climate projections: Forced response or internal variability? *Geophysical Research Letters*, *45*(20), 11390–311398. https://doi.org/10.1029/2018gl079764

Meehl, G. A., Goddard, L., Boer, G., Burgman, R., Branstator, G., Cassou, C., et al. (2014). Decadal climate prediction: An update from the trenches. *Bulletin of the American Meteorological Society*, *95*(2), 243–267. https://doi.org/10.1175/bams-d-12-00241.1

Meehl, G. A., Hu, A., & Teng, H. (2016). Initialized decadal prediction for transition to positive phase of the Interdecadal Pacific Oscillation. *Nature Communications*, *7*(1), 11718. https://doi.org/10.1038/ncomms11718

Meehl, G. A., Richter, J. H., Teng, H., Capotondi, A., Cobb, K., Doblas-Reyes, F., et al. (2021). Initialized Earth System prediction from subseasonal to decadal timescales. *Nature Reviews Earth & Environment*, *2*(5), 340–357. https://doi.org/10.1038/s43017-021-00155-x

Merryfield, W. J., Baehr, J., Batte, L., Becker, E. J., Butler, A. H., Coelho, C. A. S., et al. (2020). Current and emerging developments in subseasonal to decadal prediction. *Bulletin of the American Meteorological Society*, *101*(6), E869–E896. https://doi.org/10.1175/bams-d-19-0037.1

Milly, P. C., Malyshev, S. L., Shevliakova, E., Dunne, K. A., Findell, K. L., Gleeson, T., et al. (2014). An enhanced model of land water and energy for global hydrologic and earth-system studies. *Journal of Hydrometeorology*, *15*(5), 1739–1761. https://doi.org/10.1175/jhm-d-13-0162.1

Mishra, A. K., Ines, A. V., Das, N. N., Khedun, C. P., Singh, V. P., Sivakumar, B., & Hansen, J. W. (2015). Anatomy of a local-scale drought: Application of assimilated remote sensing products, crop model, and statistical methods to an agricultural drought study. *Journal of Hydrology*, *526*, 15–29. https://doi.org/10.1016/j.jhydrol.2014.10.038

Muñoz-Sabater, J., Dutra, E., Agustí-Panareda, A., Albergel, C., Arduini, G., Balsamo, G., et al. (2021). ERA5-Land: A state-of-the-art global reanalysis dataset for land applications. *Earth System Science Data*, *13*(9), 4349–4383. https://doi.org/10.5194/essd-13-4349-2021

Neelin, J. D., Langenbrunner, B., Meyerson, J. E., Hall, A., & Berg, N. (2013). California winter precipitation change under global warming in the Coupled Model Intercomparison Project phase 5 ensemble. *Journal of Climate*, *26*(17), 6238–6256. https://doi.org/10.1175/jcli-d-12-00514.1

Newman, M., Alexander, M. A., Ault, T. R., Cobb, K. M., Deser, C., Di Lorenzo, E., et al. (2016). The Pacific decadal oscillation, revisited. *Journal of Climate*, *29*(12), 4399–4427. https://doi.org/10.1175/jcli-d-15-0508.1

Newman, M., Compo, G. P., & Alexander, M. (2003). ENSO-forced variability of the Pacific decadal oscillation. *Journal of Climate*, *16*(23), 3853–3857. https://doi.org/10.1175/1520-0442(2003)016<3853:EVOTPD>2.0.CO;2

Pegion, K., Kirtman, B. P., Becker, E., Collins, D. C., LaJoie, E., Burgman, R., et al. (2019). The subseasonal experiment (SubX): A multimodel subseasonal prediction experiment. *Bulletin of the American Meteorological Society*, *100*(10), 2043–2060. https://doi.org/10.1175/bams-d-18-0270.1

Penland, C., & Sardeshmukh, P. D. (1995). The optimal growth of tropical sea surface temperature anomalies. *Journal of Climate*, *8*(8), 1999–2024. https://doi.org/10.1175/1520-0442(1995)008<1999:togots>2.0.co;2

Pierce, D. W., Cayan, D. R., Goodrich, J., Das, T., & Munevar, A. (2022). Evaluating global climate models for hydrological studies of the upper Colorado River Basin. *JAWRA Journal of the American Water Resources Association*, *58*(5), 709–734. https://doi.org/10.1111/1752-1688.12974

Power, S., Lengaigne, M., Capotondi, A., Khodri, M., Vialard, J., Jebri, B., et al. (2021). Decadal climate variability in the tropical Pacific: Characteristics, causes, predictability, and prospects. *Science*, *374*(6563), eaay9165. https://doi.org/10.1126/science.aay9165

Rodgers, K. B., Lee, S.-S., Rosenbloom, N., Timmermann, A., Danabasoglu, G., Deser, C., et al. (2021). Ubiquity of human-induced changes in climate variability. *Earth System Dynamics*, *12*(4), 1393–1411. https://doi.org/10.31223/X5GP79

Rohde, R. A., & Hausfather, Z. (2020). The Berkeley Earth land/ocean temperature record. *Earth System Science Data*, *12*(4), 3469–3479. https://doi.org/10.5194/essd-12-3469-2020

Schlosser, C. A., & Milly, P. C. D. (2002). A model-based investigation of soil moisture predictability and associated climate predictability. *Journal of Hydrometeorology*, *3*(4), 483–501. https://doi.org/10.1175/1525-7541(2002)003<0483:ambios>2.0.co;2

Schubert, S. D., Stewart, R. E., Wang, H., Barlow, M., Berbery, E. H., Cai, W., et al. (2016). Global meteorological drought: A synthesis of current understanding with a focus on SST drivers of precipitation deficits. *Journal of Climate*, *29*(11), 3989–4019. https://doi.org/10.1175/Jcli-D-15-0452.1

Schubert, S. D., Suarez, M. J., Pegion, P. J., Koster, R. D., & Bacmeister, J. T. (2008). Potential predictability of long-term drought and pluvial conditions in the US Great Plains. *Journal of Climate*, *21*(4), 802–816. https://doi.org/10.1175/2007jcli1741.1

Seager, R., Naik, N., & Vecchi, G. A. (2010). Thermodynamic and dynamic mechanisms for large-scale changes in the hydrological cycle in response to global warming. *Journal of Climate*, *23*(17), 4651–4668. https://doi.org/10.1175/2010jcli3655.1

Sheffield, J., Wood, E. F., & Roderick, M. L. (2012). Little change in global drought over the past 60 years. *Nature*, *491*(7424), 435. https://doi.org/10.1038/nature11575

Shi, H., Jin, F.-F., Wills, R. C., Jacox, M. G., Amaya, D. J., Black, B. A., et al. (2022). Global decline in ocean memory over the 21st century. *Science Advances*, *8*(18), eabm3468. https://doi.org/10.1126/sciadv.abm3468

Singh, A., Kumar, S., Akula, S., Lawrence, D. M., & Lombardozzi, D. L. (2020). Plant growth nullifies the effect of increased water-use efficiency on streamflow under elevated CO_2 in the Southeastern United States. *Geophysical Research Letters*, *47*(4), e2019GL086940. https://doi.org/10.1029/2019gl086940

Singh, J., Ashfaq, M., Skinner, C. B., Anderson, W. B., Mishra, V., & Singh, D. (2022). Enhanced risk of concurrent regional droughts with increased ENSO variability and warming. *Nature Climate Change*, *12*(2), 163–170. https://doi.org/10.1038/s41558-021-01276-3

Stevenson, S., Overpeck, J. T., Fasullo, J., Coats, S., Parsons, L., Otto-Bliesner, B., et al. (2018). Climate variability, volcanic forcing, and last millennium hydroclimate extremes. *Journal of Climate*, *31*(11), 4309–4327. https://doi.org/10.1175/jcli-d-17-0407.1

Stevenson, S., Wittenberg, A. T., Fasullo, J., Coats, S., & Otto-Bliesner, B. (2021). Understanding diverse model projections of future extreme El Niño. *Journal of Climate*, *34*(2), 449–464. https://doi.org/10.1175/jcli-d-19-0969.1

Stouffer, R. J., Eyring, V., Meehl, G. A., Bony, S., Senior, C., Stevens, B., & Taylor, K. (2017). CMIP5 scientific gaps and recommendations for CMIP6. *Bulletin of the American Meteorological Society*, *98*(1), 95–105. https://doi.org/10.1175/bams-d-15-00013.1

Sun, L., Alexander, M., & Deser, C. (2018). Evolution of the global coupled climate response to Arctic sea ice loss during 1990–2090 and its contribution to climate change. *Journal of Climate*, *31*(19), 7823–7843. https://doi.org/10.1175/jcli-d-18-0134.1

Sutton, C., Kumar, S., Lee, M.-K., & Davis, E. (2021). Human imprint of water withdrawals in the wet environment: A case study of declining groundwater in Georgia, USA. *Journal of Hydrology: Regional Studies*, *35*, 100813. https://doi.org/10.1016/j.ejrh.2021.100813

Swain, D. L., Langenbrunner, B., Neelin, J. D., & Hall, A. (2018). Increasing precipitation volatility in twenty-first-century California. *Nature Climate Change*, *8*(5), 427–433. https://doi.org/10.1038/s41558-018-0140-y

Ukkola, A. M., De Kauwe, M. G., Roderick, M. L., Abramowitz, G., & Pitman, A. J. (2020). Robust future changes in meteorological drought in CMIP6 projections despite uncertainty in precipitation. *Geophysical Research Letters*, *47*(11), e2020GL087820. https://doi.org/10.1029/2020gl087820

Yeager, S. G., Rosenbloom, N., Glanville, A. A., Wu, X., Simpson, I., Li, H., et al. (2022). The Seasonal-to-Multiyear Large Ensemble (SMYLE) prediction system using the Community Earth System Model version 2. *Geoscientific Model Development Discussions*, *15*(16), 1–42. https://doi.org/10.5194/gmd-15-6451-2022

Yun, K.-S., Lee, J.-Y., Timmermann, A., Stein, K., Stuecker, M. F., Fyfe, J. C., & Chung, E.-S. (2021). Increasing ENSO–rainfall variability due to changes in future tropical temperature–rainfall relationship. *Communications Earth & Environment*, *2*(1), 1–7. https://doi.org/10.1038/s43247-021-00108-8

Zeng, X. (2001). Global vegetation root distribution for land modeling. *Journal of Hydrometeorology*, *2*(5), 525–530. https://doi.org/10.1175/1525-7541(2001)002<0525:GVRDFL>2.0.CO;2